PHYSICAL REVIEW C VOLUME 47, NUMBER 4 APRIL 1993

Effective interaction for ^{16}O(p,p') and ^{40}Ca(p,p') at $E_p = 200$ MeV

H. Seifert,* J. J. Kelly, A. E. Feldman, B. S. Flanders,† and M. A. Khandaker
Department of Physics, University of Maryland, College Park, Maryland 20742.

Q. Chen,‡ A. D. Bacher, G. P. A. Berg, and E. J. Stephenson
Department of Physics, Indiana University, Bloomington, Indiana 47401

P. Karen, B. E. Norum, and P. Welch§
Department of Physics, University of Virginia, Charlottesville, Virginia 22901

A. Scott
Department of Physics and Astronomy, University of Georgia, Athens, Georgia 30602

(Received 30 October 1992)

Differential cross sections and analyzing powers for scattering of 200 MeV protons have been measured for states of ^{16}O up to 14.4 MeV and for states of ^{40}Ca up to 7.2 MeV of excitation. The data cover c.m. momentum transfers from approximately 0.4 fm^{-1} to 3.0 fm^{-1}. Calculations were performed using several density-dependent effective interactions in the local density approximation. Empirical effective interactions for isoscalar normal-parity transitions were fitted to elastic and inelastic scattering data for ^{16}O and ^{40}Ca either individually or simultaneously. Transition densities from electron scattering were used to minimize uncertainties due to nuclear structure. The fitted interactions were iterated to generate optical potentials self-consistently. We find that the empirical interaction, although strongly dependent on the local density, is essentially independent of target or state. We also find that the empirical interaction is reduced in strength at zero density. Finally, the results were compared with a relativistic impulse approximation model and with a recent global optical potential from Dirac phenomenology.

PACS number(s): 25.40.Ep, 25.40.Cm, 21.30.+y

I. INTRODUCTION

The effective interaction for the excitation by proton scattering of isoscalar normal-parity transitions was studied in a series of previous papers for a variety of targets and energies: ^{16}O at 135 MeV [1, 2], ^{16}O and ^{28}Si at 180 MeV [3], as well as ^{16}O and ^{40}Ca at 318 and 500 MeV [4–6]. Work at 100 MeV with ^{16}O and ^{40}Ca is reported in Ref. [7]. These studies employed an empirical effective interaction (EI) that uses a parametrization of density dependence based upon theoretical results for nuclear matter. Transition densities measured by electron scattering are used to minimize uncertainties due to nuclear structure. By fitting sufficiently large data sets which include states with transition densities that have strong interior contributions, the density dependence of the effective interaction can be determined with little ambiguity. It was found that even at the higher energies the effective interaction depends strongly upon local density and that essentially unique interactions can be found which describe the data for all normal-parity isoscalar states of a particular target at a given energy. Elastic and inelastic scattering can be treated consistently provided that a rearrangement contribution [8, 9] which effectively enhances the density dependence of the inelastic interaction is included. Finally, the target or A independence of the empirical interaction was demonstrated. Therefore, the basic premise of the local-density approximation (LDA) appears to be sound.

Several calculations of the effective interaction near 200 MeV have been made using the nonrelativistic theory of nuclear matter [10–16]. These models all contain the basic ingredients of Pauli blocking and binding energy corrections [17], but substantial differences in their quantitative predictions for nucleon-nucleus scattering are obtained. Although the various models employ different NN potentials, differences between approximations and numerical procedures of unknown accuracy are probably more important. Consequently, it is difficult to assess the local-density concept based upon these models alone. Therefore, Kelly *et al.* [1, 2] developed a phenomenology which is guided by theory and which can be used to

---

*Present address: Code 661, NASA-Goddard Space Flight Center, Greenbelt, MD 20771.

†Present address: Department of Physics, The American University, Washington, D.C. 20016.

‡Present address: Department of Physics, Beijing University, People's Republic of China.

§Present address: Department of Physics, Massachusetts Institute of Technology, Cambridge, MA 02139.

fit both theoretical models and data. With a physically motivated analytical form involving only a few free parameters, this empirical interaction not only facilitates the comparison of theories to each other, but also allows their quantitative comparison to a "measured" interaction for a real finite nuclear system.

It was found that the fitted empirical interactions differ in several important ways from the theoretical interactions. At 135 and 180 MeV [2, 3], the interaction at low densities is suppressed relative to the free interaction, but the subsequent density dependence is smaller than predicted by nuclear matter calculations. These differences were interpreted as evidence for nonlocal effects which might enhance the density dependence in the surface and reduce the density dependence in the interior compared with infinite nuclear matter of corresponding local density. For energies above 300 MeV [4–7], on the other hand, the empirical medium modifications appear to be considerably stronger than predicted by nonrelativistic theories. In particular, absorption, which is damped at lower energies due to Pauli blocking, now seems to be enhanced. It has been speculated that this could be due to a new absorption mechanism which is not present in the existing theories and which may be associated with the pion threshold.

Alternatively, the relativistic impulse approximation (RIA) provides a good description of elastic scattering data for 500 MeV protons without apparent need of traditional Pauli blocking and dispersion corrections [18, 19]. The difference between relativistic and nonrelativistic impulse approximations can be interpreted in terms of the coupling to virtual $N\bar{N}$ pairs [20]. The pair contribution to the optical potential is proportional to the square of the density and hence can be represented as an effective density dependence of the interaction. The principal effect of the pair contribution thus resembles a short-range repulsive contribution to the real central interaction that is proportional to density. The IA2 model of Ottenstein, Wallace, and Tjon [21] is a relativistic impulse approximation which uses a meson-exchange model to represent the complete set of Lorentz invariants for the nucleon-nucleon interaction. At 318 and 500 MeV, we find that the empirical description of elastic scattering compares well with the IA2 version of the relativistic impulse approximation [21]. Therefore, the pair contribution may be responsible for the increased density dependence relative to nonrelativistic models in this energy regime. However, since the medium modifications that are included in the nonrelativistic LDA models (NRLDA) are absent from the RIA and are more important at lower energies, comparisons with our phenomenology at 200 MeV should prove very instructive.

Finally, Dirac phenomenology (DP) [18, 22] has been shown to provide a very successful fit to elastic scattering data for broad ranges of mass and energy using global parametrizations of Dirac scalar and vector potentials. For example, Hama *et al.* [22] performed a global fit to a large database of elastic scattering data for $A \geq 40$ and $65 \leq E_p \leq 1040$ MeV. We have compared the EI and DP models at 318 and 500 MeV using equivalent Schrödinger optical potentials; although qualitatively similar, significant quantitative differences were found [5, 6]. This comparison is now extended to 200 MeV.

We have measured cross section and analyzing power distributions for many states of ^{16}O and ^{40}Ca excited by 200 MeV protons and have fitted empirical effective interactions to the data. The experiment and data analysis are described in Sec. II. The reaction model, the various models of the effective interaction, the empirical interaction, and the fitting procedure are discussed in Sec. III. NRLDA calculations using the various theoretical interactions are compared with the data in Sec. IV A. The results for the empirical effective interaction are presented in Sec. IV B. The empirical interaction is compared with relativistic models in Sec. IV C. Finally, in Sec. V we summarize our conclusions.

II. EXPERIMENT

All the data presented here were accumulated during two run periods, nine months apart, with a 200 MeV polarized proton beam at the Indiana University Cyclotron Facility (IUCF) as part of the first experiment to use the new high-resolution K600 spectrometer. A detailed description of the experiment, the diagnostic and development work, the calibration procedures, and the data analysis can be found in Ref. [7] and references therein. In the following, we present a brief summary.

A. Experimental procedure and calibrations

Beam from the polarized ion source was accelerated to the final energy in two isochronous cyclotrons. The beam energy, measured at the first bending magnet after extraction from the main-stage cyclotron, was in the range 201.4 ± 0.2 MeV. The total beam charge was measured with a Faraday cup downstream from the target. Since no continuous on-line polarimeter was available, the beam polarization was monitored periodically by lowering a ^{4}He gas cell into the beam line segment between the injector and main-stage cyclotrons. The left-right asymmetry for both beam orientations was measured with surface-barrier detectors which were positioned symmetrically on either side of the beam line. Typically polarizations of 72–77 % for spin up and 74–79 % for spin down were obtained.

The K600 spectrometer is of the quadrupole-dipole-dipole type and operates in momentum-loss configuration. For optimum resolution the spectrometer dispersion is matched with the beam line. Furthermore, the K600 provides two special poleface windings designed to correct kinematic broadening and aberration for a selected reaction. Several spectrometer acceptances from 0.6 to 3.2 msr could be defined with a set of exchangeable solid brass apertures which were mounted in a cassette between the scattering chamber and the spectrometer entrance. The detector array consisted of two multiwire vertical drift chambers (VDC's), the first of which was positioned approximately along the focal plane, and two plastic scintillators. The scintillators were used as two ΔE detectors for particle identification, provided the event trigger, and also gave the start signal for the wire TDC's.

The position and angle of particle trajectories in the focal plane were deduced from the drift distances to the VDC sense wires, which in turn were derived from the measured drift times via an empirical look-up table. Since the intrinsic efficiency for each wire is near 100%, events which triggered the scintillators but fired fewer than two wires in either chamber were classified as background and were rejected. Only events which had a good hit pattern and fired at least two consecutive wires were retained. Although two-hit events are more difficult to treat due to a left-right ambiguity, acceptance of such events was found to be essential for a flat focal-plane efficiency. The left-right ambiguity is resolved by comparison of the track information in the two chambers. We defined the chamber efficiency in terms of all the events which passed a number of software cuts and those events which additionally made a good hit pattern. With this definition the efficiency was generally between 95 and 100 %. A "clutter" correction was applied to the cross sections to account for the rate-dependent fraction of events in which multiple hits were recorded by any multiplexer, which was generally less than 2%.

The isotopically enriched (>99.9%) ^{40}Ca target was a metallic foil with an areal thickness of 15.2 mg/cm^2. The BeO target had a thickness of 22.3 mg/cm^2. We estimate the uncertainties in these thicknesses to be about ±3%. To minimize losses in resolution due to straggling, the targets were usually oriented in transmission geometry, with the target normal bisecting the scattering angle.

The scattering angle was calculated from the nominal spectrometer angle, the angle of the scattered particle at the target, and the "scattering angle offset," a quantity which describes the overall alignment of the beam and the spectrometer. The angle at the target was reconstructed in software from the measured focal plane angle via an empirical transformation polynomial. The scattering angle offset was determined by fitting the differential recoil of ^{9}Be with respect to ^{16}O, and then correcting for the fact that the spectrometer was set for ^{16}O kinematics. With this method we found offsets of 0.06°–0.19°.

The stability of measured cross sections with respect to dead time, spectrometer acceptance, relative focal-plane efficiency, and accuracy of the charge integration in the Faraday cup was thoroughly investigated. Although the data rate was generally lower than 300 Hz, we verified that dead time corrections were accurate up to 1 kHz. The effect of the other factors was found to be less than 2% and was well within the observed general reproducibility of cross section measurements, which, with a few exceptions, fluctuated between 2 and 3 %.

For scattering angles less than 18°, the spectrometer intercepts the beam line downstream of the scattering chamber and makes it necessary to place a small Faraday cup inside the scattering chamber. Unfortunately, the close proximity of the internal cup to the target creates considerable background in the spectra for forward angles. Since the internal cup is incapable of collecting all the beam charge, the data were normalized to the external cup standard, which is believed to be accurate to about 1%. A comparison of cross sections which were taken during the first run period with the external cup with those acquired in the second run period with the internal cup showed that the latter were systematically higher by about 12%. This figure also includes a difference in the overall normalization between the two run periods of about 7%, which was determined by comparing equivalent external cup data. The uncertainty in overall normalization is estimated to be about ±5%. The present elastic scattering data agree very well with previous data for ^{16}O from IUCF [23] and for ^{40}Ca from TRIUMF [24].

B. Data analysis

During replay several cuts were applied to the data in software to eliminate background, as well as particles other than protons. Halo events coming from the beam pipe and events from slit scattering were identified unambiguously by their scattering angle, which differed significantly from that of valid events. Finally, we reconstructed the particle trajectory angle within the focal plane in three different ways and required internal consistency for all methods.

Fitting of the spectra was performed with the line-shape fitting code ALLFIT [25]. The search code employs a Poisson rather than a Gaussian goodness-of-fit criterion, and thus avoids the underfitting of low-statistics data which often is a problem with the standard Gaussian criterion [26, 27]. The fitting function is composed of a background $B(x)$ and a sum of individual peaks $y_i(x)$, such that

$$y(x) = B(x) + \sum_{i=1}^{N} y_i(x), \tag{1}$$

where x is the laboratory momentum. The background function can be up to third order, and can contain two piecewise-continuous segments for targets with a decay threshold. Each peak can be described as the convolution

$$y_i(x) = I_i(x) \otimes R_i(x) \tag{2}$$

of an intrinsic line shape $I(x)$ with a resolution function $R(x)$ which represents the effects of spectrometer aberrations, target thickness, kinematic broadening, and beam properties. The standard resolution function consists of an asymmetric hyper-Gaussian in the central region plus exponential tails [26, 1]. States with negligible intrinsic width were described by the resolution function alone. States with non-negligible intrinsic width were described by Lorentzian line shapes convoluted with the resolution function. The Lorentzian line shape is appropriate for resonances within a few widths of the reaction threshold. Small peaks or unresolved peaks in multiplets could be extracted by locking their positions and shapes together, or to those of strong nearby peaks. Examples are the 0_2^+ state of ^{16}O, which was always locked to the 3_1^- peak, and the doublet and triplet clusters in ^{40}Ca.

The threshold for all the low-lying ^{9}Be peaks is at 1.665 MeV ($^9\text{Be} \rightarrow {}^8\text{Be} + n$). Although the broad structure near 6.5 MeV in ^{9}Be is known to contain at least two peaks of similar width [28–30], this region was described by a single Lorentzian peak of variable position and width because the beryllium continuum was not of primary interest for the present experiment. A threshold of 7.162 MeV, corresponding to the decay $^{16}\text{O} \rightarrow {}^{12}\text{C} + \alpha$, is appropriate for most of the ^{16}O states. An exception is the 0_2^- state for which a threshold of 12.128 MeV, corresponding to $^{16}\text{O} \rightarrow {}^{15}\text{N} + p$, was assumed to apply. The 2_3^+ state of ^{16}O at 11.52 MeV with $\Gamma = 69$ keV [31] is an example of a strong state with non-negligible intrinsic width. A fit to this state with the resolution function alone would be too narrow and thus would have underestimated the true cross section. Except as noted above, the excitation energies, widths, and thresholds used in the fitting procedure were taken from the standard compilations [32, 33].

Figures 1 and 2 show representative fitted spectra for BeO and ^{40}Ca. Resolutions better than 20 keV were achieved with the thin targets used for the tuneup, but thicker targets were used in the experiment. The resolution was typically 50–80 keV for the thicker BeO target, and 30–50 keV for the thinner ^{40}Ca target. The 0_2^+ excited state of ^{40}Ca, though weak, is clearly visible. The abrupt rise in the backgound of the BeO spectrum is due to the aforementioned decay threshold for ^{9}Be. Noticeable are the strong asymmetry of the $\frac{1}{2}{}_1^+$ state, which is only 15 keV above the threshold, and the broad unresolved Lorentzian peak [28] which is prominent in the continuum region.

We measured differential cross sections and analyzing powers for a total of 25 states of ^{16}O up to 14.4 MeV and for a total of 21 states of ^{40}Ca up to 7.2 MeV of excitation. In addition, data were obtained for the seven lowest states of ^{9}Be, some of which were previously reported in Ref. [34]. The data cover scattering angles in the laboratory between 6° and 55°, corresponding to c.m. momentum transfers between about 0.4 and 3.0 fm^{-1}. Complete data tables are available from the Physics Auxiliary Publication Service [35]. In this paper we consider only the isoscalar normal-parity states for which ground state and transition charge densities from independent electroexcitation measurements [36, 37, 31, 38, 39] are available. These include the 0_1^+ (0.0 MeV), 0_2^+ (6.049 MeV), 0_3^+ (12.053 MeV), 1_1^- (7.117 MeV), 2_1^+ (6.917 MeV), 2_2^+ (9.847 MeV), 2_3^+ (11.521 MeV), 3_1^- (6.130 MeV), and 4_1^+ (10.353 MeV) states of ^{16}O, and the 0_1^+ (0.0 MeV), 0_2^+ (3.352 MeV), 2_1^+ (3.904 MeV), 3_1^- (3.736 MeV), 3_2^- (6.286 MeV), 3_3^- (6.583 MeV), and 5_1^- (4.492 MeV) states of ^{40}Ca.

III. MODELS OF THE EFFECTIVE INTERACTION

A. Reaction model

Direct, one-step reactions can be conveniently treated within the single-scattering framework using a local $t\rho$ folding model, whereby the scattering amplitude is constructed from the effective nucleon-nucleon interaction weighted by the nucleon distribution inside the target nucleus. In general, the evaluation of the complete amplitude for a transition is difficult due to the implied sum over charge indices and the variety of possible densities and interaction components involved [40]. For the special case of isoscalar normal-parity transitions in self-conjugate nuclei, charge symmetry ensures that $\rho_n = \rho_p$ to a good approximation. Furthermore, when the transverse form factors measured with electron scattering are negligible, the matter density and interaction dominate [41]. Thus, in the notation of Ref. [4], the scattering potential reduces to the form

$$U(\mathbf{r}) = U^Z(\mathbf{r}) + U^C(\mathbf{r}) + \nabla F^{LS}(\mathbf{r}) \times \frac{1}{i}\nabla \cdot \boldsymbol{\sigma}, \quad (3)$$

where U^Z is the potential which is obtained by folding the Coulomb interaction with the transition charge density. The central and spin-orbit multipole potentials

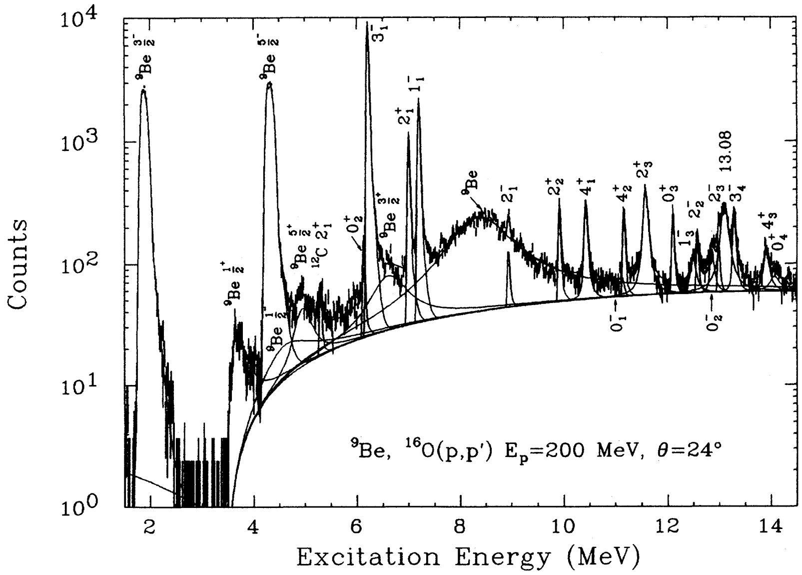

FIG. 1. Sample fitted spectrum for scattering of 200 MeV protons through 24° by a BeO target. In addition to the total fit, separate contributions are shown for the background and for each peak.

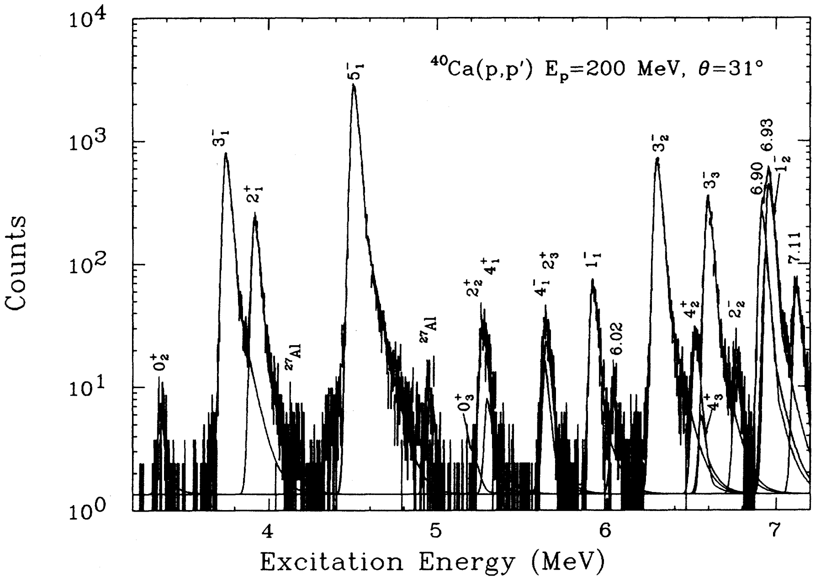

FIG. 2. Sample fitted spectrum for scattering of 200 MeV protons through 31° by a ^{40}Ca target. In addition to the total fit, separate contributions are shown for the background and for each peak.

$$U_J^C(r) = \eta \frac{2}{\pi} \int dq\, q^2 j_J(qr) \tilde{t}^C(q, \rho_g(r)) \tilde{\rho}_J(q), \tag{4a}$$

$$F_J^{LS}(r) = \eta \frac{2}{\pi} \int dq\, q^2 j_J(qr) \tilde{\tau}^{LS}(q, \rho_g(r)) \tilde{\rho}_J(q), \tag{4b}$$

are obtained by folding the matter transition densities $\tilde{\rho}_J$ with the central and spin-orbit components of the effective interaction, $\tilde{t}^C$ and $\tilde{\tau}^{LS}$. Note that for convenience we define $t^{LS} = -(k^2 \sin\theta)\tau^{LS}$. The Jacobian η relates the interactions in the NN and NA frames [42, 43]. Exchange is treated in the zero-range exchange approximation and the local wave number is calculated from the asymptotic energy [44]. Similarly, the spherical optical potential for elastic scattering is

$$U(r) = U^Z(r) + U^C(r) + U^{LS}(r)\mathbf{L} \cdot \boldsymbol{\sigma}, \tag{5}$$

where the spin-orbit component is related to the scattering potential by

$$U^{LS}(r) = \frac{1}{r} \frac{\partial F^{LS}}{\partial r}. \tag{6}$$

The proton densities are obtained by unfolding the nucleon form factor from charge densities measured by electron scattering and charge symmetry is used to equate neutron and proton densities. Ground-state densities were obtained from Refs. [36, 37]. Transition densities were obtained from Ref. [31] for ^{16}O and from Refs. [38, 39] for ^{40}Ca. Following Ref. [1], and using the simplest implementation of the LDA, the density dependence of the interaction is evaluated with the local ground-state density $\rho_g(r)$ at the projectile position.

Although the same effective interaction is used to generate both the optical and scattering potentials, the density dependence of the interaction for inelastic scattering is effectively doubled by the rearrangement factor $(1 + \rho\partial/\partial\rho)$ which was first derived for nucleon scattering by Cheon *et al.* [8, 9]. For the entire energy range between 135 and 500 MeV, this factor has previously [1–6] been found to be essential to a consistent description of both elastic and inelastic scattering by a common interaction.

B. Effective interactions

Three theoretical models of the effective interaction for the scattering of 200 MeV protons are available. Two of the models choose the nuclear matter approach [17] to construct a complex and density-dependent interaction. In the case of the Paris-Hamburg (PH) interaction [13, 14], the correlated pair wave function in nuclear matter is evaluated using the Paris potential [45] and a local effective interaction in pseudopotential form is constructed using a method [12, 46] based on the averaging procedure of Siemens [47]. This method simulates to a certain degree the properties of the correlated wave function, including its short-range behavior, and hence, important off-shell amplitudes due to anticorrelation effects at short distances are retained at least on average. The Nakayama-Love (NL) interaction [15] is based on the Bonn potential [48] and uses a pseudopotential prescription which is designed to reproduce the on-shell matrix elements of the full nuclear matter calculation. Although these interactions employ different NN input potentials, the large differences between them are more likely due to the very different procedures used to reduce nonlocal nuclear matter results to local forms amenable to scattering calculations. The third interaction is the low-energy extension of a model due to Ray [16], who evaluated the medium modifications to the Watson optical model [49] using a nucleon-isobar coupled channels model [50–52] which explicitly includes inelasticities in the NN, $N\Delta(1232)$, and $NN^*(1440)$ channels. It also includes Pauli blocking and binding potentials for intermediate nucleon and isobar states but, unlike the PH and NL models, it does not include the projectile optical potential in the energy denominator of the propagator.

Since these interactions are available from the authors only as voluminous tables of amplitudes or Yukawa expansion coefficients, it is often more convenient to use instead the parametrization which was introduced in Refs. [1, 2]:

$$t_i(q,\kappa_F) = (S_i - d_i\kappa_F^{\alpha_i})\, t_i^{(f)}(q) + \kappa_F^{\gamma_i} q^{\delta_i} \sum_{n=1}^{N} a_{in} y^{\beta_i}(q/\mu_{in}). \qquad (7)$$

Here, $\kappa_F = k_F/1.33$ represents the local Fermi momentum relative to saturation, $t^{(f)}(q)$ is the free interaction at zero density, $y(x) = (1+x^2)^{-1}$ is a Yukawa function, and the μ_{in} are various mass parameters which are chosen to optimize the fit to component i. Theoretical interactions require the scale factors S_i to be unity, although they may be allowed to vary in empirical analyses of scattering data. If the individual components of the interaction are interpreted as Fourier transforms of Yukawa expansions [1], one finds that the natural exponents β are 1 for central, 2 for spin-orbit, and 3 for tensor interactions. Similarly, $\delta = 2$ for tensor interactions and $\delta = 0$ otherwise. The density dependence of the real central part of the interaction is best described by the addition of a short-ranged repulsive core, due to the anticorrelation between identical nucleons, which enhances the differential cross section at large momentum transfer. The amplitude of the core contribution is proportional to the density, such that $\gamma_1 = 3$. The effect of Pauli blocking upon the imaginary central part of the interaction is suppression of the forward cross section. A simple phase-space model due to Clementel and Villi [53] predicts $\alpha_2 = 2$ and $d_2 \propto E_0^{-1}$.

The relevant interaction components for the three models are compared in Figs. 3 and 4. For the PH and NL interactions the fits (lines) are displayed along with the original interactions (symbols). The free interactions for these fits were obtained by extrapolating the respective effective interactions to zero density. The Love-Ray (LR) interaction is treated somewhat differently. For this model, Ray [16] computed the medium modifications to the free interaction using a theoretical model, and then added these modifications to a phenomenological t matrix based on Arndt phase shifts [54]. Following Refs. [4–6], we replace this phenomenological t matrix with the commonly used FL t matrix of Franey and Love [55]. Hence, the LR interaction which is shown in Figs. 3 and 4 consists of the fitted medium modifications applied to the FL t matrix.

The fitted parameters for all three models are collected in Table I. The most significant differences between the three interactions can be found in the central components. Both the strength and the range of the repulsive core in the real central component are smaller for the NL model than for the PH or LR models. The shorter range makes the density dependence of the NL interaction almost independent of momentum transfer and causes the curves in Fig. 3 to remain almost parallel even at large momentum transfers. The repulsive core is considerably stronger for the PH than for the LR or NL models. On the other hand, the damping of the imaginary component

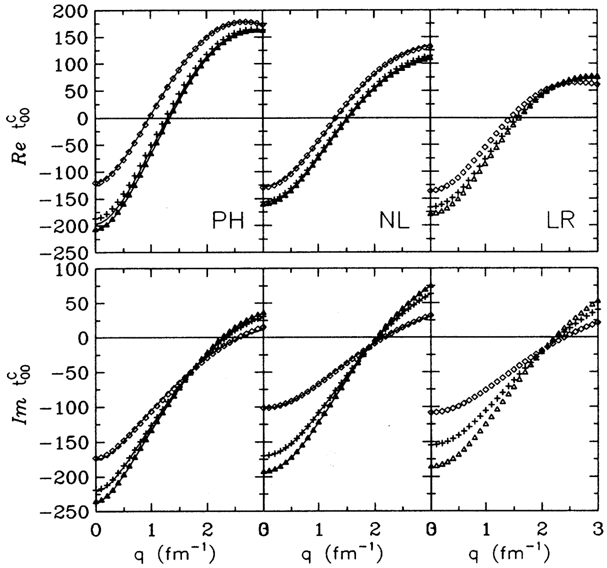

FIG. 3. Isoscalar spin-independent central components of the PH, NL, and LR effective interactions. The symbols show the original interactions for k_F = 0.6 fm^{-1} (triangles), 1.0 fm^{-1} (crosses), and 1.4 fm^{-1} (diamonds). The curves in each panel represent two parameter fits to the respective interaction. The LR interaction is only shown in its reparametrized form, with its original free interaction replaced by the FL t matrix.

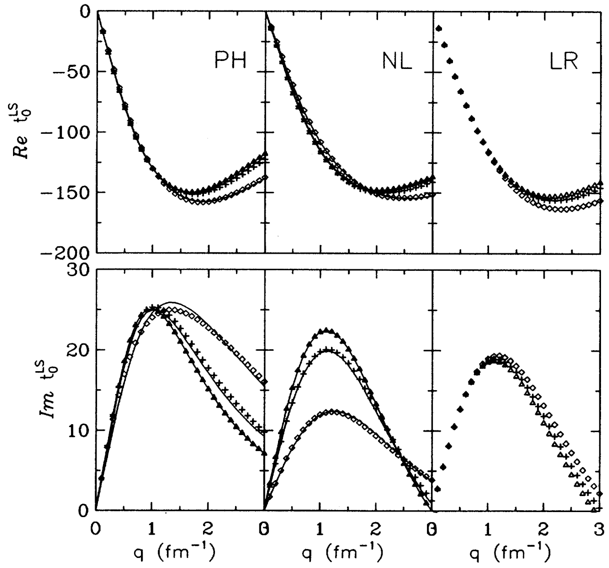

FIG. 4. Isoscalar spin-orbit components of the PH, NL, and LR effective interactions. Note that $t_0^{LS} = -(k^2 \sin\theta)\tau_0^{LS}$ in the notation of Ref. [1]. The symbols show the original interactions for k_F = 0.6 fm^{-1} (triangles), 1.0 fm^{-1} (crosses), and 1.4 fm^{-1} (diamonds). The curves in each panel represent two parameter fits to the respective interaction. The LR interaction is only shown in its reparametrized form, with its original free interaction replaced by the FL t matrix.

TABLE I. Reparametrization of 200 MeV theoretical interactions.

Component	Coefficient	μ^{a}	$[\alpha\gamma\beta\delta]$	PH	NL	LR
$\mathrm{Re}t_{00}^{C}$	a_{11} (MeV fm^3)	0	[3310]	-56.7	13.7	-69.0
	a_{12} (MeV fm^3)	3.0 fm^{-1}		132.5	14.8	109.5
$\mathrm{Im}t_{00}^{C}$	d_2		[2210]	0.283	0.454	0.457
	a_{21} (MeV fm^3)	0		-11.9	-5.71	-7.37
$\mathrm{Re}\tau_0^{LS}$	a_{31}(MeV fm^5)	3.0 fm^{-1}	[3320]	-6.85	-9.92	-4.94
	a_{32} (MeV fm^5)	6.0 fm^{-1}		5.86	6.30	4.64
$\mathrm{Im}\tau_0^{LS}$	d_4		[2220]	0.569	0.601	0.179
	a_{41} (MeV fm^5)	3.0 fm^{-1}		-5.30	-1.56	-1.56

[a] An entry of 0 is to be interpreted as a delta function with $\mu^{-1} = 0$.

is considerably weaker for the PH than for either the NL or LR interactions.

It is also important to observe that at low density the central components of the PH interaction are considerably stronger than those of the FL t matrix, which was fitted to nucleon-nucleon data. This difference between the interactions reflects the fact that the PH algorithm does not necessarily reduce to the free interaction at zero density, an effect which leads to rather large discrepancies between the real central components at large momentum transfers (compare also Refs. [1, 4]).

To demonstrate the effect of the density dependence on scattering observables, it is instructive to display the matter interaction

$$|t_m(q)|^2 = |t^C(q)|^2 + |t^{LS}(q)|^2, \tag{8a}$$

which in the plane-wave approximation is proportional to the cross section, and the plane-wave analyzing power

$$A_y(q) = \frac{\mathrm{Im}\left[t^C(q)t^{LS^*}(q)\right]}{|t^C(q)|^2 + |t^{LS}(q)|^2}, \tag{8b}$$

where $t^{LS} = -(k^2 \sin\theta)\tau^{LS}$. These properties of the PH, NL, and LR interactions are compared in Fig. 5. As we go from low to high densities, we observe that the cross section is increasingly suppressed for low q and enhanced at high q. Similarly, the analyzing powers are shifted towards smaller momentum transfers and are reduced for intermediate momentum transfer. However, although the density dependence is qualitatively similar for all three models, at low density the PH cross sections are considerably stronger than those of the other models.

C. Empirical interactions

An empirical interaction can be obtained by fitting data with a somewhat simpler parametrization that is designed to minimize correlations among the fitting parameters and hence to yield more stable fits than the full form, Eq. (7). Following Ref. [2], we analyze scattering data with

$$\mathrm{Re}t_{00}^{C}(q,\kappa_F) = S_1 \mathrm{Re}t_{00}^{C(f)}(q) + b_1\kappa_F^3 y(q/\mu_1), \tag{9a}$$

$$\mathrm{Im}t_{00}^{C}(q,\kappa_F) = \left[S_2 - d_2\kappa_F^2\right] \mathrm{Im}t_{00}^{C(f)}(q), \tag{9b}$$

$$\mathrm{Re}\tau_0^{LS}(q,\kappa_F) = S_3 \mathrm{Re}\tau_0^{LS(f)}(q) + b_3\kappa_F^3 y^2(q/\mu_3). \tag{9c}$$

Usually, the imaginary spin-orbit component is too weak to be fitted and is constrained to its theoretical form. The choices $\mu_1 = 1.5$ fm^{-1} and $\mu_3 = 6.0$ fm^{-1} provide fits to the PH and LR interactions which are almost as good as those in Figs. 3–5 with Eq. (7), but the fit to the NL interaction is not as good with this simpler parametrization. The simplified parametrizations are given in Table II together with the parameters fitted to data.

The fitting procedure described in Refs. [2, 5] includes a self-consistency cycle which continues until both chi squared and the parameters converge. Convergence is usually achieved in less than ten iterations. To assure that the data for all the states and observables are equally weighted throughout the fitted range of momentum transfer, additional uncertainties of ±5% are folded into cross section data and ±0.05 into analyzing power data. Of course, in our figures all the data are plotted with their original error bars. Also, the data are plotted for the entire measured range, even though the fits are restricted to $q \leq 2.7$ fm^{-1}. This restriction is made because both the electromagnetic form factors and the validity of the reaction model tend to be limited to about twice the Fermi momentum.

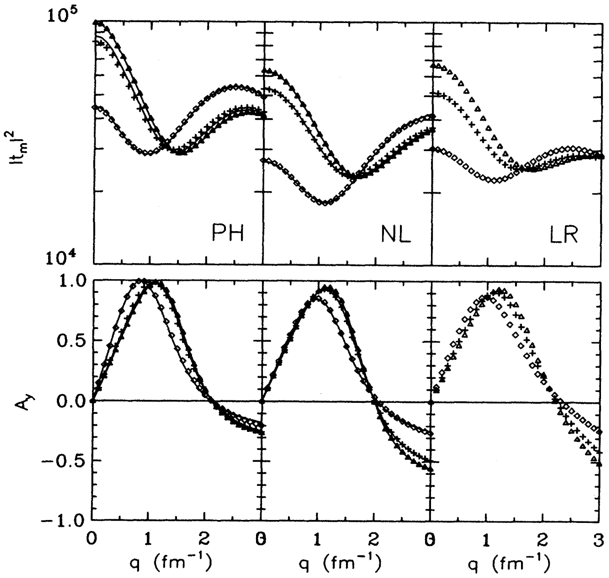

FIG. 5. Plane-wave matter interactions and analyzing powers for the PH, NL, and LR effective interactions, using the same legend as Fig. 3.

TABLE II. Fitted empirical effective interactions.

Label[a]	Data set	S_1[b]	b_1 (MeV fm^3)	S_2	d_2	S_3	b_3 (MeV fm^5)	χ^2_ν
PH	Theory	[1.0]	84.0	[1.0]	0.217	[1.0]	1.86	
PH1	^{16}O	0.652	67.2	0.763	0.099	0.850	2.41	5.1
PH2	^{40}Ca	0.672	42.9	0.826	0.175	0.829	6.17	8.1
PH3	^{16}O, ^{40}Ca	0.670	55.2	0.771	0.137	0.853	3.33	6.6
NL	Theory	[1.0]	38.6	[1.0]	0.424	[1.0]	0.514	
LR	Theory	[1.0]	34.0	[1.0]	0.422	[1.0]	1.96	
LR1	^{16}O	0.742	71.3	0.780	0.175	0.845	2.84	5.7
LR2	^{40}Ca	0.814	45.1	0.788	0.262	0.815	2.23	11.3
LR3	^{16}O, ^{40}Ca	0.795	56.7	0.768	0.222	0.833	2.31	8.3

[a] Here $\mu_1 = 1.5$ fm^{-1} and $\mu_3 = 6.0$ fm^{-1}; the components Imτ_0^{LS} are fixed to their theoretical values.

[b] Square brackets indicate a fixed parameter.

IV. RESULTS

All the cross section and analyzing power data which are used and presented in this section are from this work. Additional data for the spin rotation functions (SRF) are taken from Ref. [24]. To enhance detail, the elastic cross sections are always presented as ratios to the point-charge Rutherford cross section (σ_R). All the calculations employ consistent distorted waves emanating from optical potentials based upon the same effective interactions used for inelastic scattering. Note that use of optical potentials fitted to elastic scattering data does not significantly alter any of the comparisons among the interactions. The transition densities are taken from electron scattering. The density dependence of the effective interaction is now so well established in this energy regime that it is no longer necessary to include impulse approximation calculations based upon the free interaction.

A. Local-density approximation

LDA calculations are compared with elastic scattering data in Fig. 6 and with inelastic data in Figs. 7–11. The three calculations shown use the original PH (solid) and NL (short dashes) interactions, and the reparametrized form of the LR (long dashes) interaction with the FL *t* matrix. The differences among the various LDA interactions are qualitatively smaller at 200 MeV than at lower energies. Although it had been previously observed for other energies up to 318 MeV [1, 3, 4] that the PH interaction provides the best overall description of the data, the preference for that interaction at 200 MeV is slight. Furthermore, it also appears that the NL interaction is much more successful at this energy than at lower energies. Although both the NL and LR interactions describe the elastic cross sections for this energy slightly better than the PH interaction, at low *q* they systematically un-

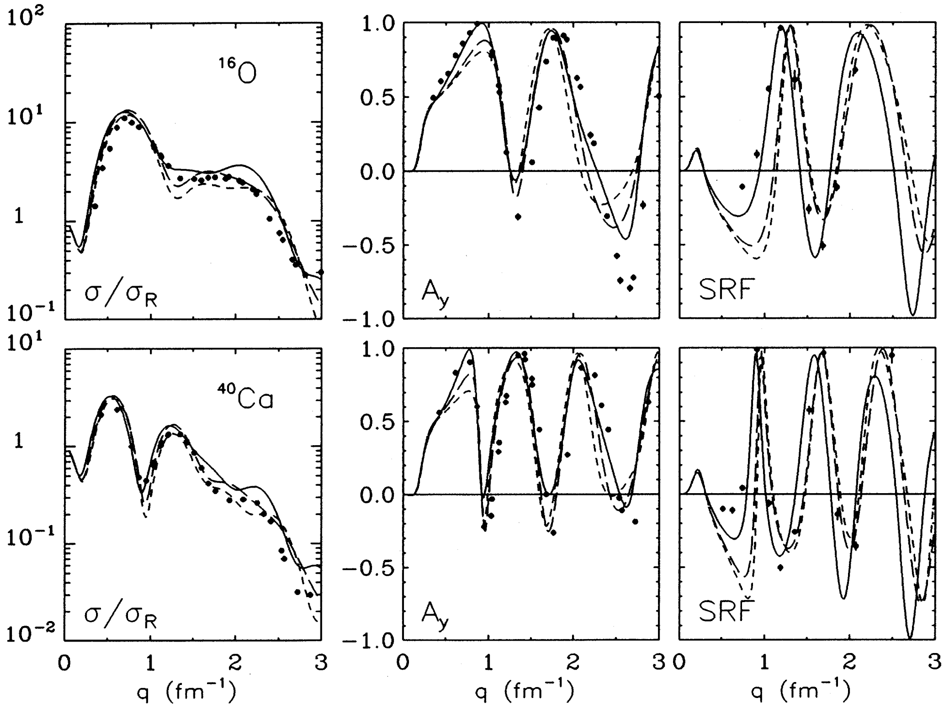

FIG. 6. LDA calculations based upon the PH (solid), NL (short dashes), and LR (long dashes) interactions are compared with 200 MeV elastic scattering data for ^{16}O and ^{40}Ca. Elastic cross sections are presented as ratios to the Rutherford cross section (σ_R) to enhance detail. The spin-rotation function data are from Ref. [24].

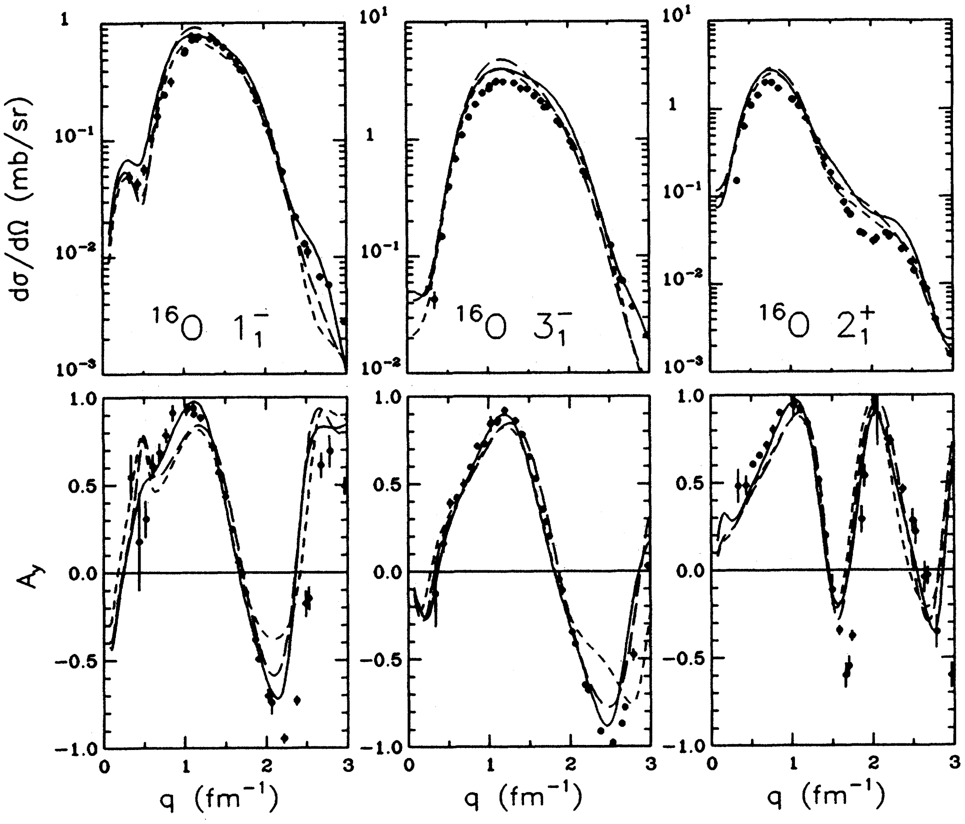

FIG. 7. LDA calculations based upon the PH (solid), NL (short dashes), and LR (long dashes) interactions are compared with 200 MeV data for the 1_1^-, 3_1^-, and 2_1^+ states of ^{16}O.

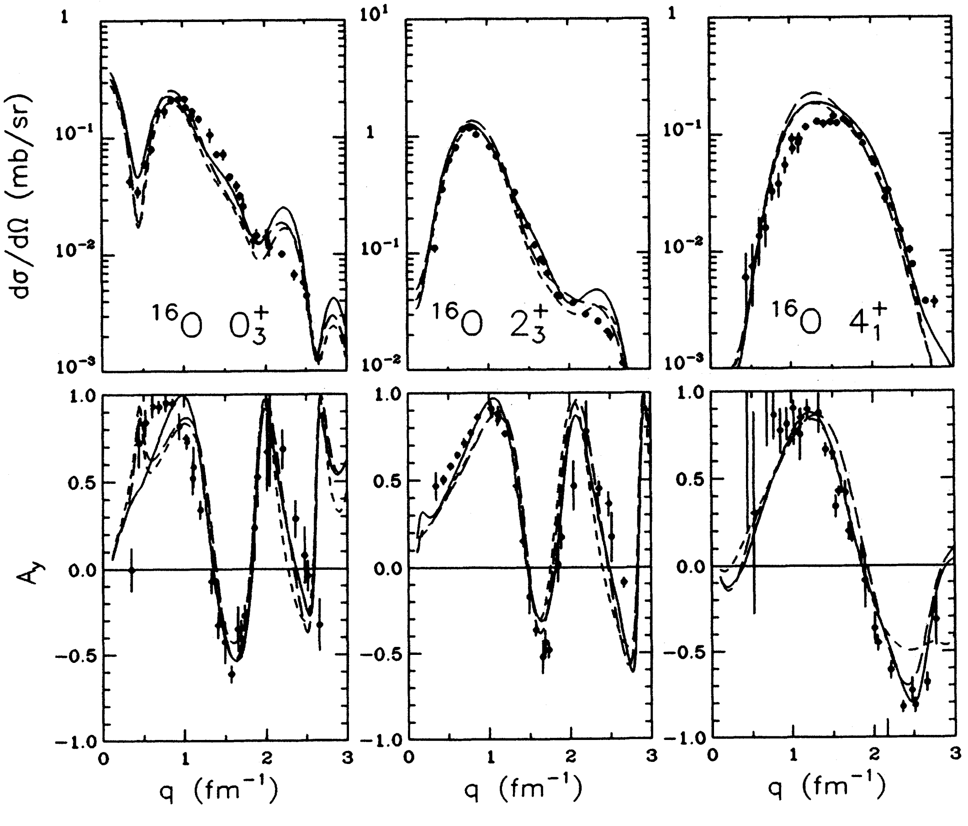

FIG. 8. LDA calculations based upon the PH (solid), NL (short dashes), and LR (long dashes) interactions are compared with 200 MeV data for the 0_3^+, 2_3^+, and 4_1^+ states of ^{16}O.

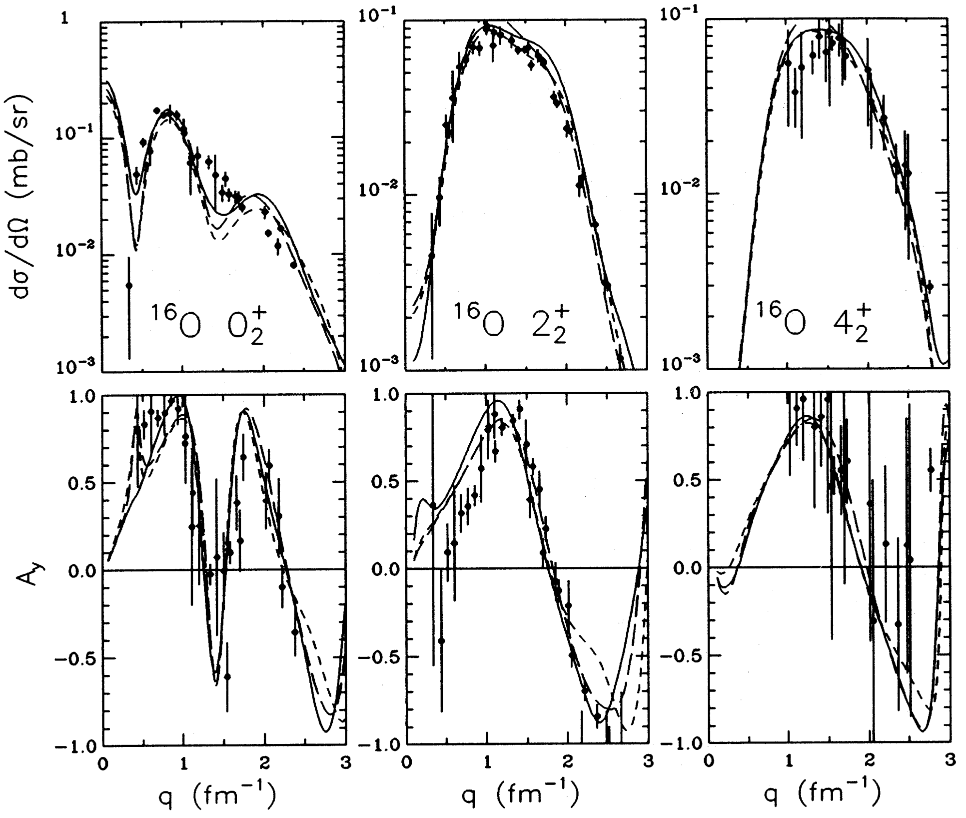

FIG. 9. LDA calculations based upon the PH (solid), NL (short dashes), and LR (long dashes) interactions are compared with 200 MeV data for the 0_2^+, 2_2^+, and 4_2^+ states of ^{16}O. The 4_2^+ data include an unresolved 3^+ state.

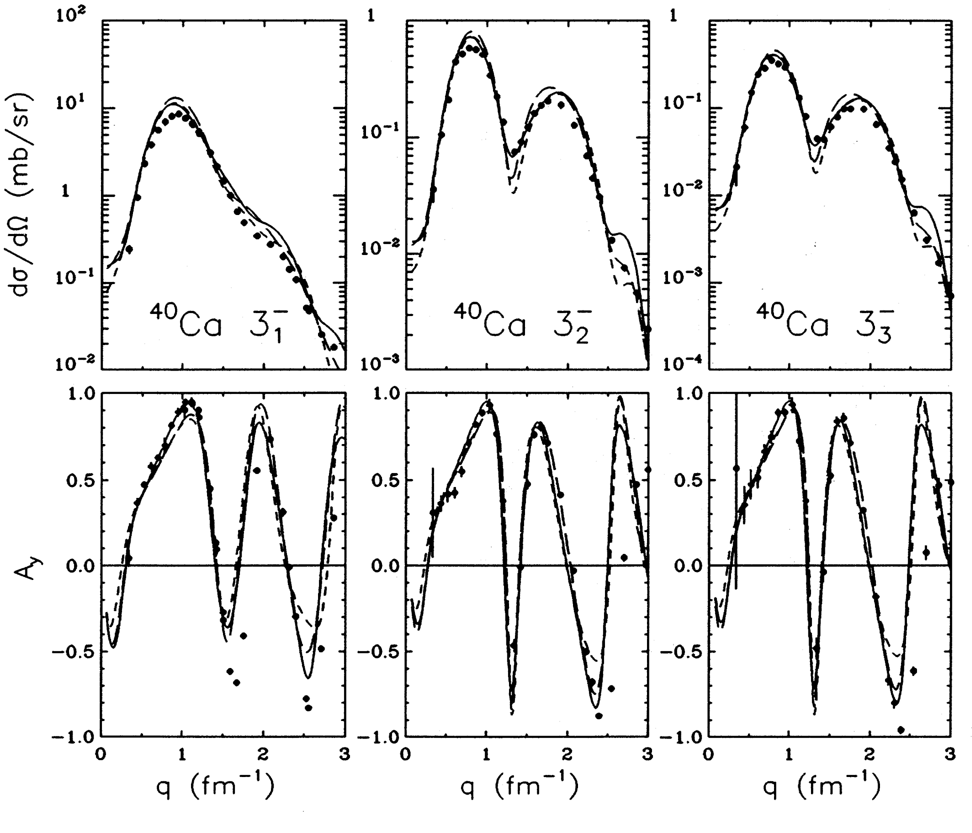

FIG. 10. LDA calculations based upon the PH (solid), NL (short dashes), and LR (long dashes) interactions are compared with 200 MeV data for the 3_1^-, 3_2^-, and 3_3^- states of ^{40}Ca.

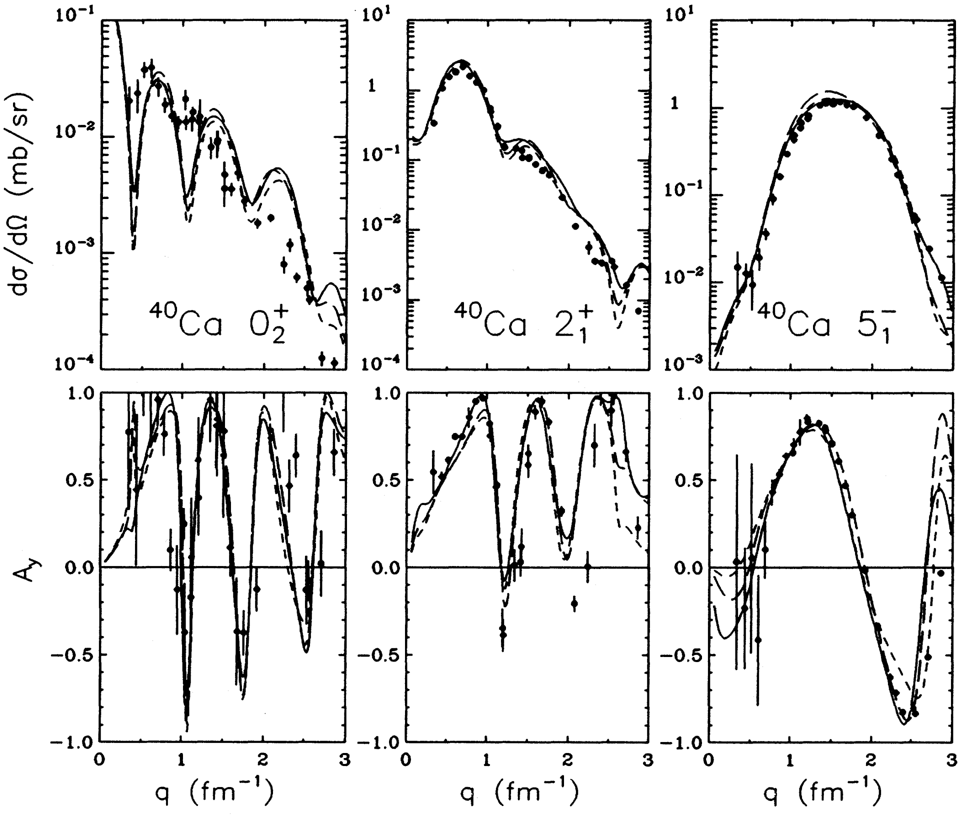

FIG. 11. LDA calculations based upon the PH (solid), NL (short dashes), and LR (long dashes) interactions are compared with 200 MeV data for the 0_2^+, 2_1^+, and 5_1^- states of ^{40}Ca.

derestimate the analyzing powers. This effect is already apparent in the comparison of the analyzing powers near $k_F \approx 1.4$ fm^{-1} that is shown in Fig. 5 for these interactions. The observation that for surface-peaked states, such as the 2_1^+ state of ^{16}O or the 3_1^- state of ^{40}Ca, all the models overestimate the peak cross sections suggests that the interaction has to be reduced for low densities. The observation that interior states, such as the 1_1^- state of ^{16}O or the 3_2^- state of ^{40}Ca, are described reasonably well by the models suggests that for consistency the overall density dependence of such a scaled interaction should also be reduced.

Despite its weakness and close proximity to the 3_1^- peak, data which are well described by the LDA could be obtained for the 0_2^+ state of ^{16}O. The difficulties in reproducing the cross section for the 0_3^+ state of ^{16}O for momentum transfers near 1.5 fm^{-1} appear smaller at 200 MeV than at lower energies. Although the relative importance of omitted spin-current contributions [1, 56] is expected to decrease with energy, the data for these 0^+ states will be omitted from the fitting procedure at this energy also. Nevertheless, these data provide important tests of the effective interaction near saturation density. Similarly, the accuracy of the calculations for the 2_2^+ state of ^{16}O is also better than for lower energies, presumably because the relative contribution of multistep excitation decreases between 100 and 200 MeV. The data for the 4_2^+ state of ^{16}O may be affected by an unresolved 3^+ state but are inadequate for phenomenological analysis anyway.

Although the cross section for the 0_2^+ state of ^{40}Ca is very small, about an order of magnitude smaller than similar states of ^{16}O, the good resolution and relatively small background for the K600 spectrometer enabled good data to be obtained. The oscillations of the analyzing power angular distribution are described very well by the LDA models. However, the cross section data appear to be shifted with respect to the calculations and the deep minima which are predicted appear to be absent. Similar but less severe difficulties in calculations for this state were observed at 318 MeV also. If the cross section were to receive substantial multistep contributions, we would have expected larger discrepancies in the analyzing power calculations. We have chosen to include these data in the fitting process for the empirical effective interaction, but note that their influence upon the χ^2 search is negligible anyway.

B. Empirical effective interaction

The results of fitting the parameters of the empirical effective interaction (EI) to selected cross section and analyzing power data are tabulated in Table II. Interactions PH1, PH2, and PH3 employ the PH interaction for zero density as the free interaction, whereas interactions LR1, LR2, and LR3 employ the FL t matrix. Components which were not fitted, such as Imt^{LS}, were taken from the PH G matrix for the PHn versions (n = 1, 3) and from the LR interaction for the LRn versions of the EI, hence the choice of code names. Within each set, the first includes only the data for ^{16}O, the second ^{40}Ca, and the third both data sets simultaneously. For ^{16}O the states selected for fitting include 0_1^+ (0.0 MeV), 1_1^- (7.117 MeV), 2_1^+ (6.917 MeV), 2_3^+ (11.521 MeV), 3_1^- (6.130 MeV), and 4_1^+ (10.353 MeV). For ^{40}Ca we include 0_1^+ (0.0 MeV), 0_2^+ (3.352 MeV), 2_1^+ (3.904 MeV), 3_1^- (3.736 MeV), 3_2^- (6.286 MeV), 3_3^- (6.583 MeV), and 5_1^- (4.492 MeV). Note that very similar results are obtained for each set using only elastic or only inelastic scattering. Thus six free parameters were fitted to as many as 26 angular distributions simultaneously. The availability for both targets of a variety of transition densities, some of surface character and others with strong interior contributions, permits the density dependence of the effective interaction to be determined with relatively little ambiguity.

The A independence of the empirical effective interaction is illustrated in Figs. 12–16, where short dashes show calculations for the LR1 interaction, long dashes for LR2, and solid lines for LR3. Although slightly better results for elastic scattering are obtained with the LR1 interaction, particularly for the spin-rotation function (SRF) data which were omitted from the fits, the results for inelastic scattering are practically indistinguishable. Similarly, virtually indistinguishable results are obtained by fitting either elastic or inelastic data alone. Evidently, most of the remaining differences between the various interactions can be attributed to unresolved correlations among the parameters which do not strongly affect the scattering calculations. The fact that excellent fits to the ^{40}Ca data are obtained using interactions fitted to ^{16}O, or vice versa, supports the basic premise of the LDA that the effective interaction depends primarily upon local density and is essentially independent of either state or target. The fact that the same interactions fit elastic and inelastic scattering simultaneously supports the accuracy of the Cheon rearrangement relation.

The elastic cross section calculations fall slightly below the data in the vicinity of the second diffraction peaks for both targets. This effect was also observed for lower energies, but appears to decrease with energy and to be absent by about 300 MeV. This problem may be due to a minor inaccuracy in the Cheon rearrangement prescription or to a deficiency in the model of the effective interaction for low density. A strict interpretation of the LDA would require the effective interaction to reduce to the free t matrix at low density, but scale factors less than unity are required to fit the inelastic scattering data for energies below 300 MeV. These scale factors are closer to unity for higher energies. If the low-density interaction requires medium modifications beyond those of the LDA, there is no guarantee that simple scaling is adequate. A more complicated q-dependent adjustment could improve the fit to the elastic data. On the other hand, the inelastic calculations for surface densities tend to be slightly too strong at comparable momentum transfers, suggesting that a modification of the rearrangement relationship could help also. Also note that full-folding corrections could affect the elastic and inelastic scattering calculations differently at this level. Full-folding calculations are presently available only for elastic scattering [57–59] and exhibit changes with respect to optimal factorization which resemble those attributed to medium modifications in the LDA. However, the χ^2 fitting procedure we employ ensures that a good global fit to all of the data is obtained, possibly at the expense of obscuring subtle differences among the various transitions considered.

Additional support for the A independence of the em-

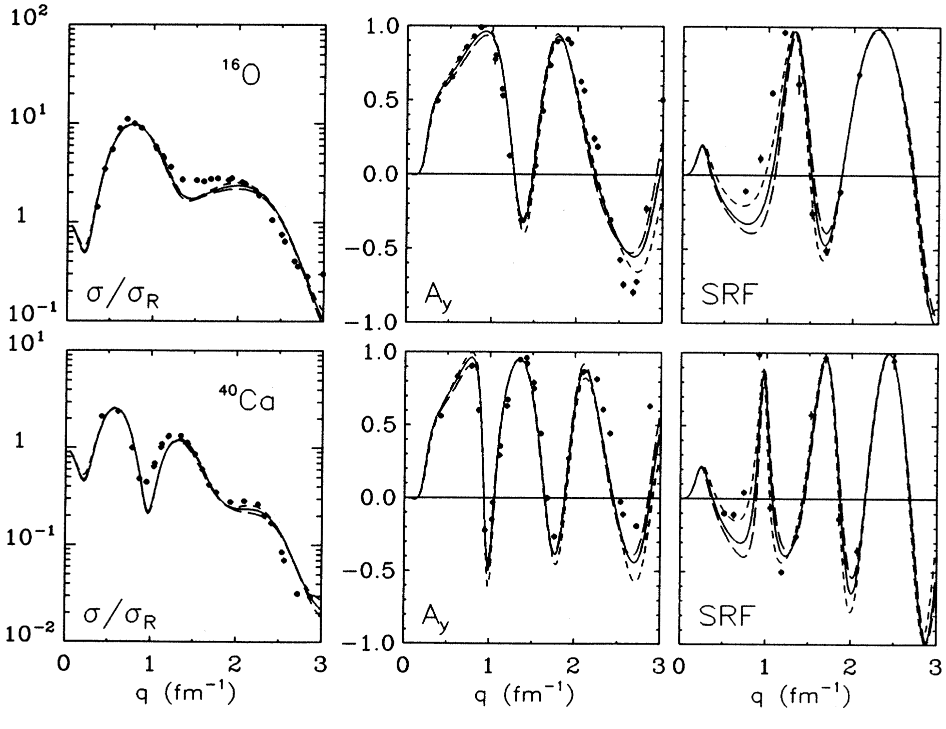

FIG. 12. A independence of the effective interaction. LDA calculations based upon the LR3 (solid), LR2 (long dashes), and LR1 (short dashes) interactions are compared with 200 MeV elastic scattering data for ^{16}O and ^{40}Ca. Elastic cross sections are presented as ratios to the Rutherford cross section (σ_R) to enhance detail. The spin-rotation function data are from Ref. [24].

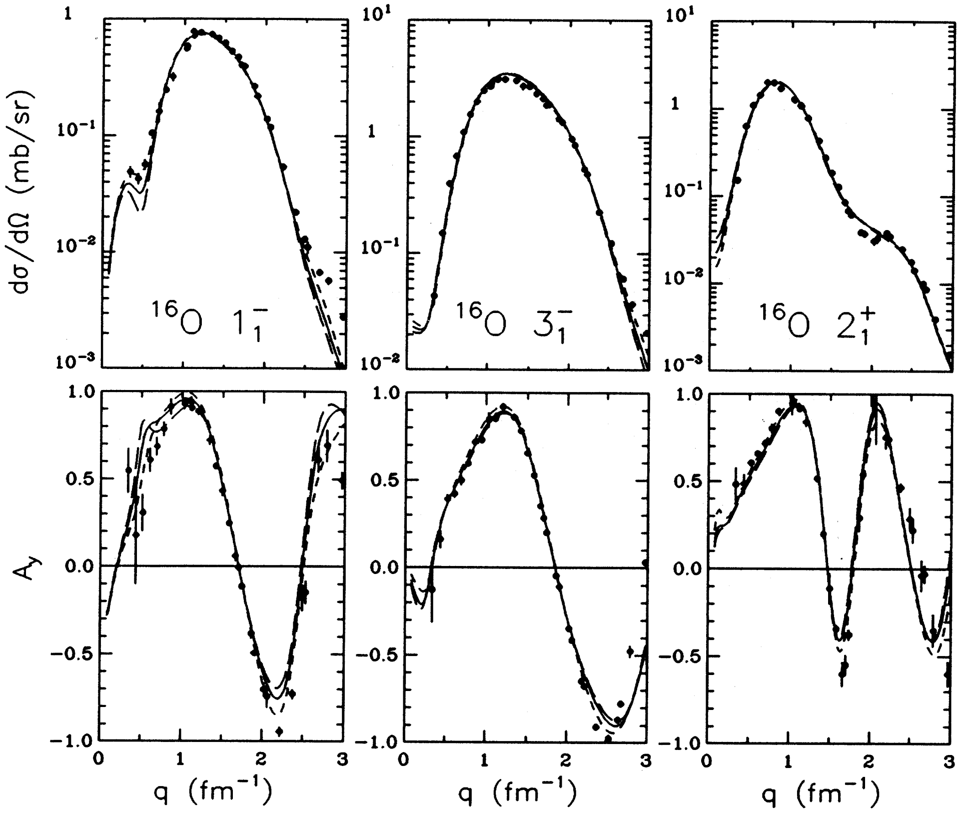

FIG. 13. A independence of the effective interaction. LDA calculations based upon the LR3 (solid), LR2 (long dashes), and LR1 (short dashes) interactions are compared with 200 MeV data for the 1_1^-, 3_1^-, and 2_1^+ states of ^{16}O.

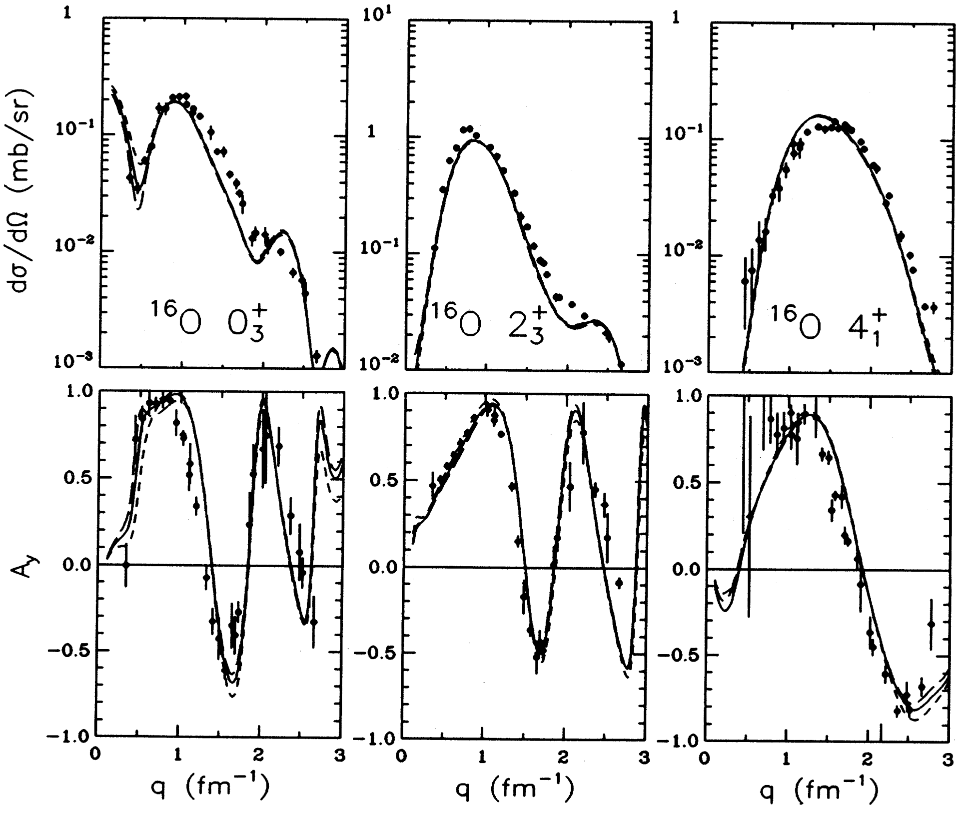

FIG. 14. A independence of the effective interaction. LDA calculations based upon the LR3 (solid), LR2 (long dashes), and LR1 (short dashes) interactions are compared with 200 MeV data for the 0_3^+, 2_3^+, and 4_1^+ states of ^{16}O.

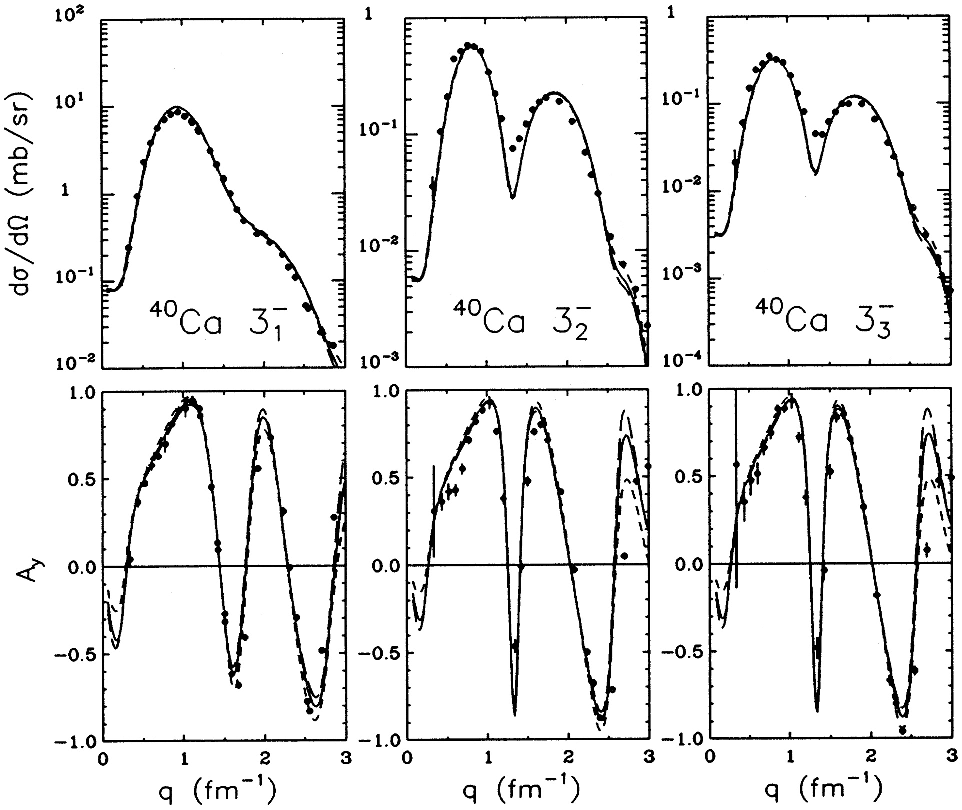

FIG. 15. *A* independence of the effective interaction. LDA calculations based upon the LR3 (solid), LR2 (long dashes), and LR1 (short dashes) interactions are compared with 200 MeV data for the 3_1^-, 3_2^-, and 3_3^- states of ^{40}Ca.

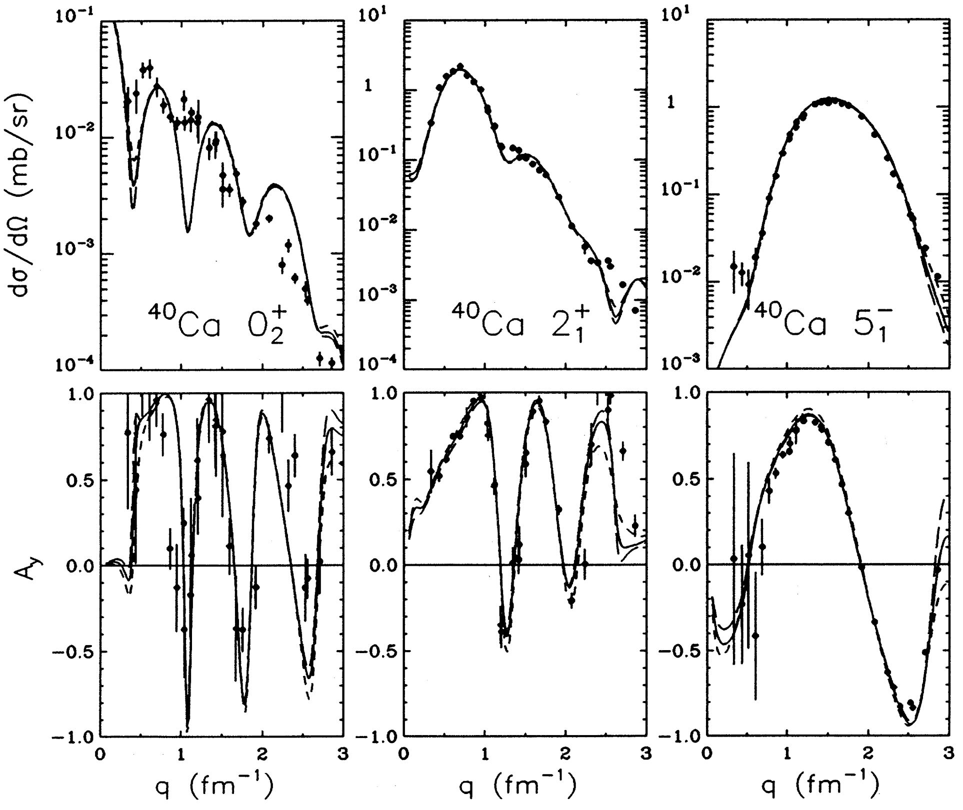

FIG. 16. *A* independence of the effective interaction. LDA calculations based upon the LR3 (solid), LR2 (long dashes), and LR1 (short dashes) interactions are compared with 200 MeV data for the 0_2^+, 2_1^+, and 5_1^- states of ^{40}Ca.

pirical effective interaction is found in the elastic scattering calculations for ^{12}C and ^{208}Pb presented in Fig. 17. The data are from Ref. [60] for ^{12}C and from Refs. [61,62] for ^{208}Pb. Densities were obtained from Ref. [63]. Short dashes show calculations based upon the FL t-matrix, long dashes the LR interaction, and solid curves the empirical effective interaction (LR3). The density dependence of the LR interaction improves the elastic scattering predictions of the impulse approximation, particularly for the analyzing power, but is not sufficient to accurately reproduce the data. Much better agreement with the data is provided by the empirical effective interaction. Not only is good agreement with the data obtained with the LR3 interaction, but the residual deviations with the data for these targets are similar to those for ^{16}O and ^{40}Ca. Also note that a microscopic coupled channels calculation based upon the empirical effective interaction gave an excellent description of the 200 MeV data for the rotational band of ^{9}Be, demonstrating that the local-density approximation is successful even for light deformed nuclei [34]. Therefore, the data are consistent with the existence of a universal density-dependent effective interaction for normal-parity isoscalar transitions and suggest that EI is a good approximation thereto.

The dependence of the empirical effective interaction upon which model of the free interaction is employed in the analysis is illustrated by the subset of calculations shown in Figs. 18–20. Although the zero-density limit of the PH interaction is significantly different from the FL t matrix, this difference does not strongly affect the quality of the fit to the data. Furthermore, the parameters listed in Table II are qualitatively similar for both analyses. The stronger $\mathrm{Re}t_{00}^{C}$ component in the PH model is compensated in part by smaller scale factors. Similarly, the damping coefficient d_2 is smaller both in the original PH interaction and in the subsequent fits based upon it than in the corresponding LR interactions. It is interesting to note that even though the FL t matrix was fitted to nucleon-nucleon data, the PH model of the t matrix seems to give slightly better fits to the nucleon-nucleus scattering data at 200 MeV and at lower energies. However, these differences are small and may not be physically meaningful. Therefore, possible ambiguities in the interaction for low density do not appear to compromise the determination of the empirical effective interaction.

Useful comparisons among the nonrelativistic models of the effective interaction can be made using the optical potentials shown in Fig. 21 for ^{40}Ca. Similar results are obtained for ^{16}O. The bands represent the total spread among the six empirical effective interactions listed in Table II. The edges of these bands are largely determined by the differences between the LR1 and LR2 interactions. For example, the upper edge of the $\mathrm{Re}U^{C}$ band is largely determined by LR1 and the lower by LR2 because the real central component of the interaction has stronger density dependence when fitted to the data for ^{16}O than for ^{40}Ca. The LR3 results are near the middles of the bands and the potentials that use the PH t matrix for the free interaction are also contained within the bands. Furthermore, even though the inelastic scattering data dominate the fitting procedure, all six interactions give goods fits to the elastic data. Therefore, the widths of the bands should represent realistic uncertainties for each term of the optical potential. However, the band for $\mathrm{Im}U^{LS}$ is artificially small: since that term was not varied the band represents the difference in that component of the PH and LR interactions.

The interior uncertainty in the real central potential

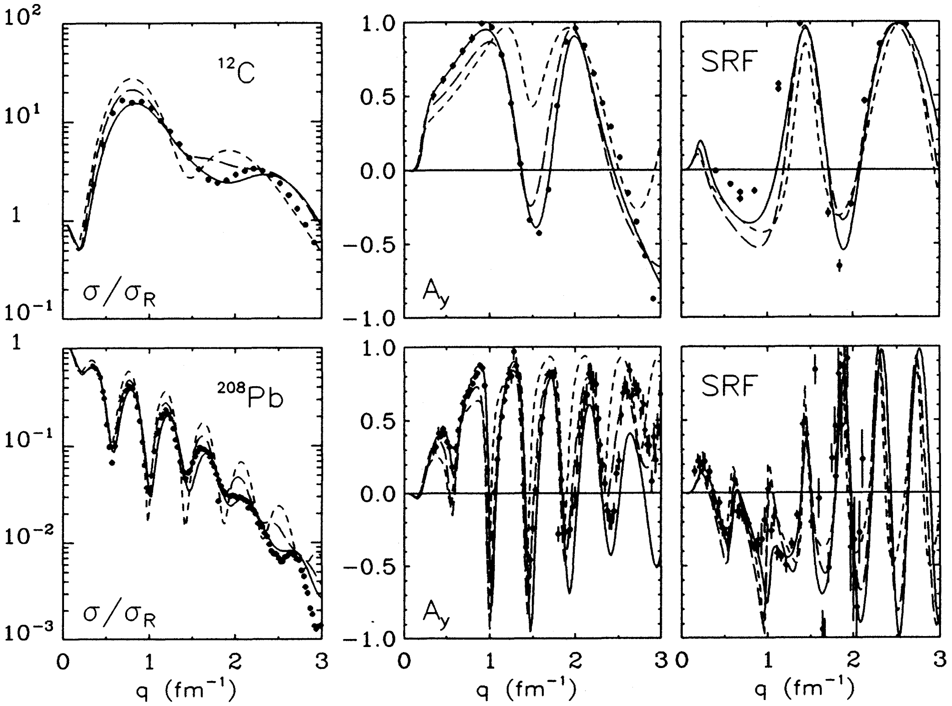

FIG. 17. A independence of the effective interaction. LDA calculations based upon the LR3 (solid), LR (long dashes), and FL (short dashes) interactions are compared with 200 MeV elastic scattering data for ^{12}C and ^{208}Pb. Elastic cross sections are presented as ratios to the Rutherford cross section (σ_R) to enhance detail. The data are from Refs. [60–62].

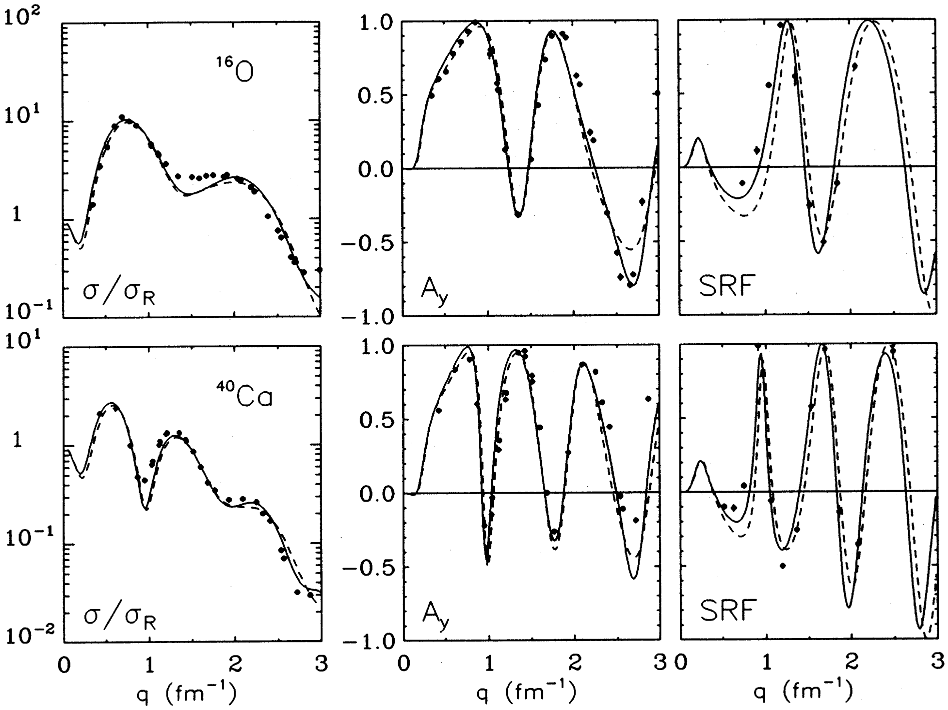

FIG. 18. Empirical interactions based upon the PH (solid) and FL (dashes) t matrices. Calculations using PH3 and LR3 are compared with 200 MeV elastic scattering data for ^{16}O and ^{40}Ca. Elastic cross sections are presented as ratios to the Rutherford cross section (σ_R) to enhance detail. The spin-rotation function data are from Ref. [24].

is relatively large because the real part is weaker than the imaginary part in the interior and its effectiveness is reduced by absorption. This effect increases with energy. Analyses of the empirical effective interaction at 318 and 500 MeV have shown that the parameters of the imaginary central interaction are determined with smaller variations due to the choice of data set or model than are the parameters of the real central interaction [4–6]. Thus, in the interior the range of real central potentials compatible with the data increases with energy, but the potential

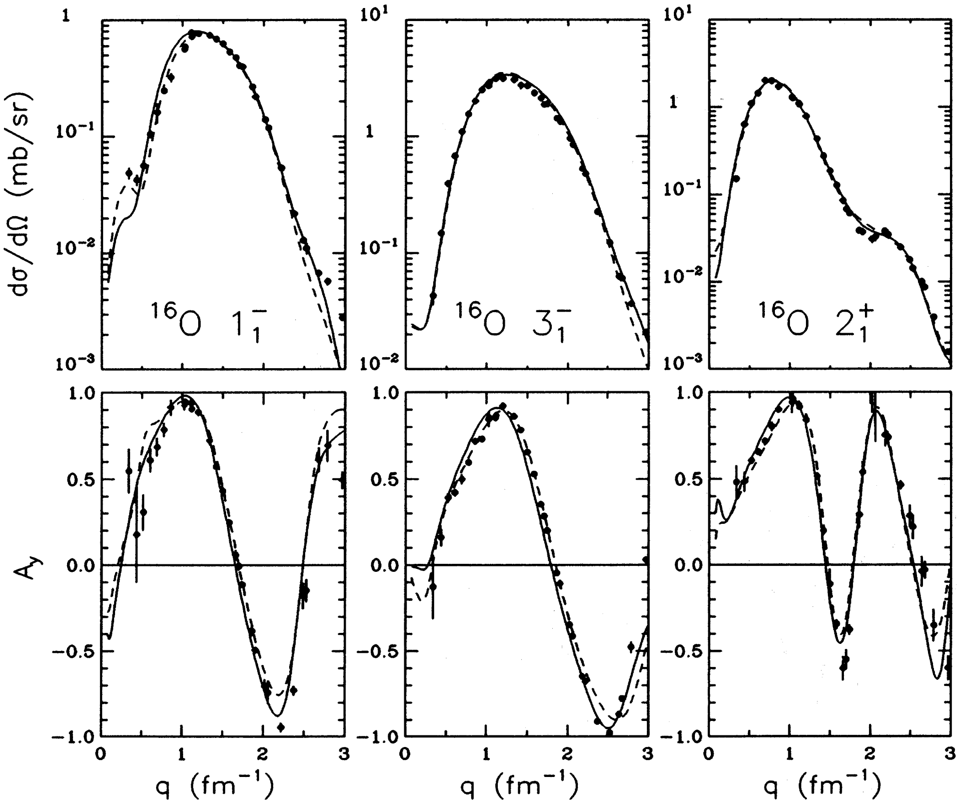

FIG. 19. Empirical interactions based upon the PH (solid) and FL (dashes) t matrices. Calculations using PH3 and LR3 are compared with 200 MeV data for the 1_1^-, 3_1^-, and 2_1^+ states of ^{16}O.

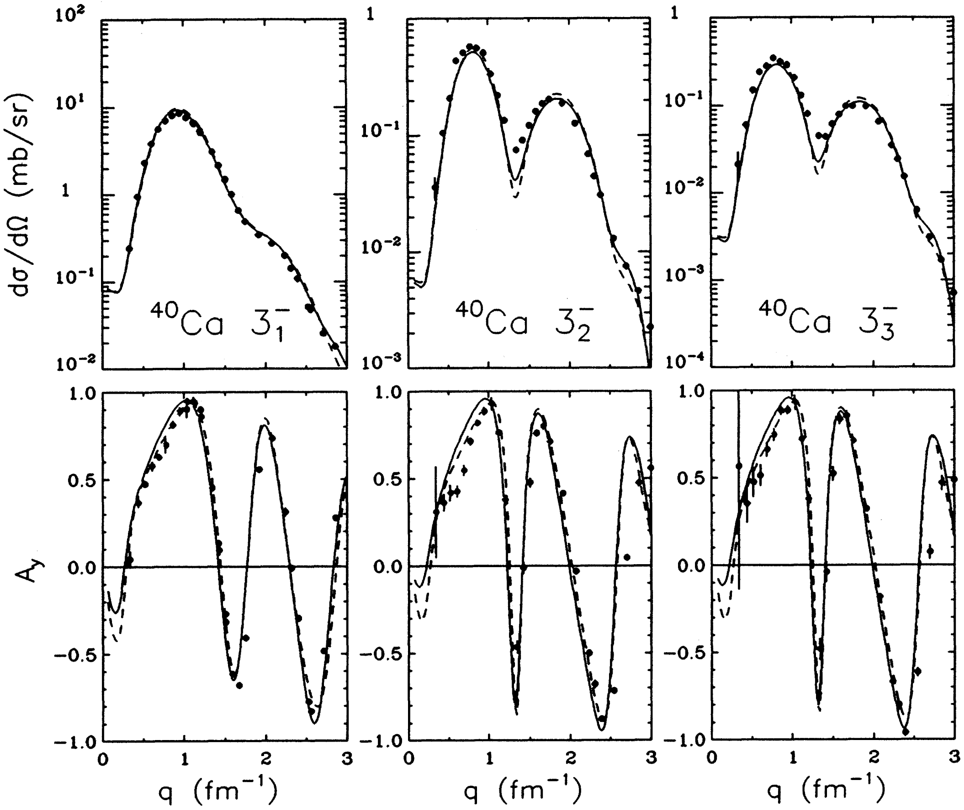

FIG. 20. Empirical interactions based upon the PH (solid) and FL (dashes) t matrices. Calculations using PH3 and LR3 are compared with 200 MeV data for the 3_1^-, 3_2^-, and 3_3^- states of ^{40}Ca.

in the surface region remains well determined.

The density dependence for Ret_{00}^C is smaller in the NL and LR models than in the PH model and consequently their ReU^C potentials are stronger also. The density dependence for that component of EI is intermediate, so that the radial dependence of the potential is smoother than in the PH model. Also note that at low density the PH model for Ret_{00}^C is stronger than the other interactions, so that the tail of ReU^C is strongest for that model. However, the suppression of the free interaction, indicated by $S_1 < 1$, reduces ReU^C so that EI produces the weakest real central potential. The scale factor is smallest when EI is based upon the PH t matrix to compensate for the stronger free interaction. Thus, the net difference with respect to the impulse approximation is strongest for the empirical effective interaction even though the density dependence is intermediate between the PH and LR models.

The absorptive potential for the EI model is consistent with the NL and LR predictions, but is somewhat weaker than the PH model. The PH model has the smallest damping coefficient d_2, whereas the other models all have similar values for that parameter. Although d_2 is smaller for EI than for NL or LR, similar absorptive potentials are obtained because $S_2 < 1$. These parameters tend to be highly correlated for elastic scattering, but good fits to inelastic scattering for both interior and surface transition densities require $S_2 < 1$ with the present parametrization.

The real spin-orbit potentials are similar for all models. The imaginary spin-orbit potential is too small to

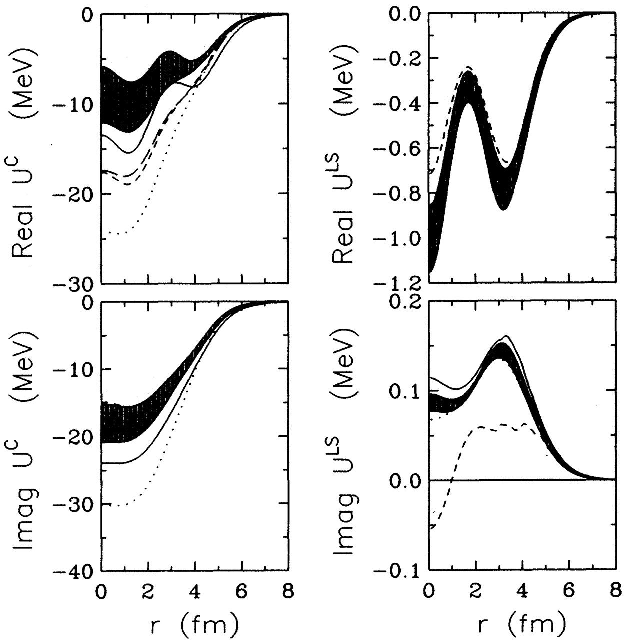

FIG. 21. Optical potentials for ^{40}Ca(p,p) at 200 MeV in the local-density approximation are shown for the EI (band), PH (solid), NL (short dashes), and LR (long dashes) interactions. Note that the NL and LR curves for the imaginary central potential lie almost entirely within the shaded band. Impulse approximation results using the FL t matrix (dots) are also shown for comparison.

fit to the data, but all models except NL produce similar results for that component. The somewhat irregular features present in the NL model for that component probably indicate that some numerical instabilities were encountered in the extraction of that component of the effective interaction from the nuclear matter calculation.

C. Comparison with relativistic models

In this section we compare the present nonrelativistic phenomenolgy with relativistic models by means of the equivalent Schrödinger optical potentials, which are illustrated in Fig. 22 for ^{40}Ca. The bands show the spread among the effective interactions fitted to data. Two relativistic models have been considered. The solid lines represent the ^{40}Ca optical potential from the global Dirac phenomelogy (DP) of Hama *et al.* [22], here designated as DP1 for "fit 1." For the IA2 model of Ottenstein, Wallace, and Tjon [21], the dotted curves show the *no-pairs* (NP) limit in which the contribution of virtual $N\bar{N}$ pairs is neglected, whereas the dashes show the full IA2 result.

The NP calculations are essentially equivalent to the nonrelastivic impulse approximation (NRIA). In the IA2 model the dominant contribution of virtual $N\bar{N}$ pairs is equivalent to a short-ranged repulsive contribution to the real central component of the effective interaction. At 200 MeV, this effect is considerably stronger than predicted by nonrelativistic theories of nuclear matter and than fitted to data using the empirical effective interaction. There is also a significant enhancement in ReU^{LS} due to the density dependence of the IA2 model. However, without explicit inclusion of Pauli blocking in the IA2 model, the absorptive potential remains much stronger than for the nonrelativisitic models which include Pauli blocking.

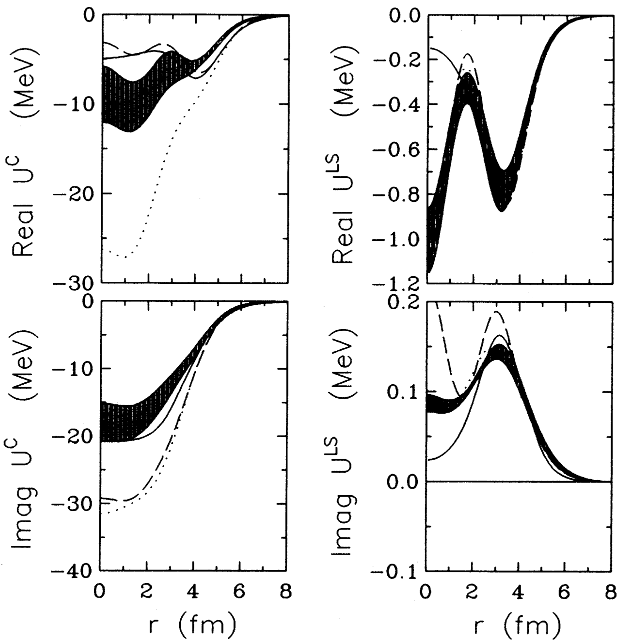

FIG. 22. The optical potential for ^{40}Ca(p,p) at 200 MeV from the empirical interaction (band) is compared with the DP1 (solid), full IA2 (dashes), and NP (dots) optical potentials.

Elastic scattering calculations using the IA2 model are compared with the LR3 and DP1 models in Fig. 23. Although the density dependence of Ret^C_{00} improves the IA2 analyzing power calculations considerably, compared with the NP result, the cross section calculations remain much stronger than the data, particularly for large momentum transfer. For low q this deficiency in the IA2 model can be attributed primarily to the absence of Pauli blocking. Murdock and Horowitz [64] found that with a reasonable *ad hoc* correction for Pauli blocking, considerably better agreement with elastic scattering data could be obtained using a simpler version of the RIA. For high q the problem is probably due to excessively strong repulsion in Ret^C_{00} at this energy. The IA2 model is more successful near 500 MeV where Pauli blocking is not as important and where the density dependence in Ret^C_{00} is similar to that of the empirical effective interaction [6]. The comparison between these models for 318 MeV, shown in Ref. [5], represents an intermediate case.

The DP1 elastic scattering calculations are also shown in Fig. 22. These data were not included in the data base of Hama *et al.* [22], but an excellent fit is obtained nonetheless and most components of the DP1 potential are consistent with the EI bands. Although the scalar and vector Dirac potentials were parametrized with simple functions similar to the traditional Woods-Saxon form, the real central potential has a more com-

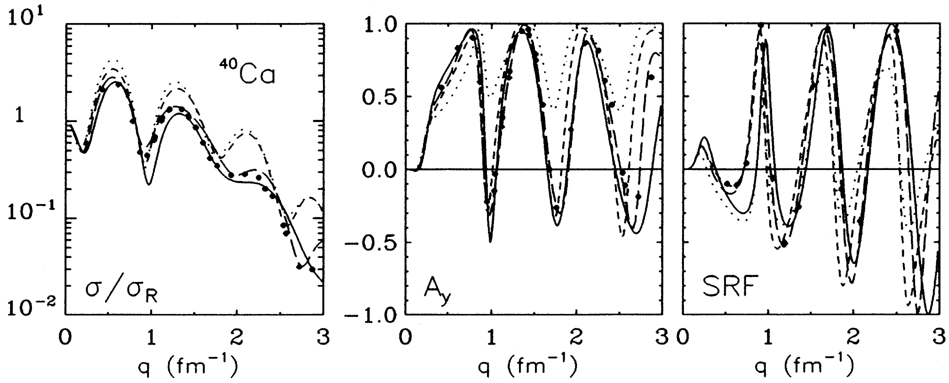

FIG. 23. Calculations based upon the empirical effective interaction LR3 (solid), and the DP1 (long dashes), full IA2 (short dashes), and NP (dots) optical potentials are compared with 200 MeV elastic scattering data for ^{40}Ca. The elastic cross sections are presented as ratios to the Rutherford cross section (σ_R) to enhance detail. The spin-rotation function data are from Ref. [24].

plicated radial dependence that results from near cancellation of two terms with different geometries. The empirical effective interaction produces a similar radial dependence using the density dependence of the effective interaction within a finite nucleus with nonuniform density. The low-density suppression of Ret_{00}^{C}, represented by the S_1 parameter, is apparently responsible for the weaker tail in the EI model for ReU^C. Since the DP1 model gives a better fit to the elastic data, whereas $S_1 < 1$ is required to fit the inelastic data, there may be some residual difference between elastic and inelastic interactions that is not adequately described by the Cheon rearrangement relation.

V. CONCLUSIONS

We have obtained cross section and analyzing power data for the scattering of 201.4 MeV protons by ^{16}O and ^{40}Ca, including many states up to 14.4 MeV excitation for the former and 7.2 MeV for the latter. Empirical effective interactions for normal-parity isoscalar transitions were fitted to the data for both targets individually and simultaneously. Transition densities measured with electron scattering were used to minimize uncertainties due to nuclear structure. The availability of a wide range of transition densities, including some of surface character and others with strong interior contributions, permits the density dependence of the effective interaction to be unfolded from the data with little ambiguity. Thus, by comparing interactions fitted to data for several nuclei the hypothesis that the effective interaction depends primarily upon local density can be tested.

We obtain good agreement between the interactions fitted to data for ^{16}O and ^{40}Ca either individually or simultaneously. This result supports the local-density hypothesis. We also find little sensitivity to details of the parametrization of the free interaction, obtaining similar interactions based upon the PH or FL t matrices. Furthermore, similar results are obtained by fitting elastic or inelastic scattering, either individually or simultaneously. Therefore, the empirical effective interaction was determined with only minor ambiguities due to parameter correlations. The spread among the optical potentials that result from the various effective interactions that were fitted to the data provides a useful measure of the uncertainties in these potentials. The potentials were compared with both relativistic and nonrelativistic models.

The density dependence we find for Ret_{00}^{C} at 200 MeV is intermediate between the PH and LR models and much smaller than that of the IA2 model. For Imt_{00}^{C} we find that the Pauli blocking coefficient is similar to that of PH model and significantly smaller than in the NL or LR models. Nevertheless, the density dependence of Imt_{00}^{C} remains important at 200 MeV. For Ret_{0}^{LS} the density dependence of the empirical effective interaction is slightly stronger than predicted by the nonrelativistic nuclear matter models. However, as previously found for lower energies, good fits to the inelastic scattering data for states with surface-peaked transition densities require the interaction to be reduced at low density more strongly than would be expected using the local-density approximation. For ReU^C this suppression reinforces the density dependence so that the net difference with respect to the free interaction is larger for the empirical effective interaction than for any of the nonrelativistic theories of nuclear matter. For ImU^C the net effect of reduced damping and low-density suppression produces absorptive potentials similar to the LR or NL models, but improves the inelastic scattering calculations. The need for modifications at low density probably indicates that an extension of the LDA is required for finite nuclei. In finite nuclei, the density dependence of the effective interaction appears to be stronger at low density and weaker at high density than for infinite nuclear matter of corresponding density.

The similarity between optical potentials calculated from the empirical effective interaction and those fitted with Dirac phenomenology suggests that the empirical effective interaction can describe the density dependence due to relativisitic effects, such as coupling to virtual $N\bar{N}$ pairs, in addition to that due to essentially nonrelativistic medium modifications, such as Pauli blocking and dispersion. The latter should be incorporated into future versions of the relativistic impulse approximation and at low energy will probably be as important as for nonrelativistic models. Without these corrections, the density dependence of the IA2 interaction is too strong in the real part and too small in the imaginary part of the central interaction for 200 MeV, but is similar to the empirical effective interaction for 500 MeV where the density dependence of nonrelativistic interactions is too small. Therefore, it appears that both sources of density dependence will need to be included self-consistently in future theoretical models which seek to explain the energy dependence of the empirical effective interaction. Furthermore, full-folding and/or finite-nucleus corrections must be developed more thoroughly.

ACKNOWLEDGMENTS

We thank Dr. L. Ray for tables of his effective interaction and Dr. N. Ottenstein and Prof. S. J. Wallace for the IA2 optical potential. We thank W. Loszowski for assistance with the targets and members of the IUCF staff for their efforts during the commissioning of the K600 spectrometer. This work was supported in part by grants from the National Science Foundation and the U. S. Department of Energy. One of the authors, H. Seifert, acknowledges the National Research Council-NASA/GSFC for financial support.

---

[1] J. J. Kelly, W. Bertozzi, T. N. Buti, J. M. Finn, F. W. Hersman, C. Hyde-Wright, M. V. Hynes, M. A. Kovash, B. Murdock, B. E. Norum, B. Pugh, F. N. Rad, A. D. Bacher, G. T. Emery, C. C. Foster, W. P. Jones, D. W. Miller, B. L. Berman, W. G. Love, J. A. Carr, and F. Petrovich, Phys. Rev. C **39**, 1222 (1989).
[2] J. J. Kelly, Phys. Rev. C **39**, 2120 (1989).
[3] J. J. Kelly, W. Bertozzi, T. N. Buti, J. M. Finn, F. W.

Hersman, C. Hyde-Wright, M. V. Hynes, M. A. Kovash, B. Murdock, P. Ulmer, A. D. Bacher, G. T. Emery, C. C. Foster, W. P. Jones, D. W. Miller, and B. L. Berman, Phys. Rev. C **41**, 2504 (1990); Q. Chen, J. J. Kelly, P. P. Singh, M. C. Radhakrishna, W. P. Jones, and H. Nann, *ibid.* **41**, 2514 (1990); J. J. Kelly, Q. Chen, P. P. Singh, M. C. Radhakrishna, W. P. Jones, and H. Nann, *ibid.* **41**, 2525 (1990).

[4] J. J. Kelly, A. E. Feldman, B. S. Flanders, H. Seifert, D. Lopiano, B. Aas, A. Azizi, G. Igo, G. Weston, C. Whitten, A. Wong, M. V. Hynes, J. McClelland, W. Bertozzi, J. M. Finn, C. E. Hyde-Wright, R. W. Lourie, P. E. Ulmer, B. E. Norum, and B. L. Berman, Phys. Rev. C **43**, 1272 (1991).

[5] J. J. Kelly, P. Boberg, A. E. Feldman, B. S. Flanders, M. A. Khandaker, S. D. Hyman, H. Seifert, P. Karen, B. E. Norum, P. Welch, S. Nanda, and A. Saha, Phys. Rev. C **44**, 2602 (1991).

[6] B. S. Flanders, J. J. Kelly, H. Seifert, D. Lopiano, B. Aas, A. Azizi, G. Igo, G. Weston, C. Whitten, A. Wong, M. V. Hynes, J. McClelland, W. Bertozzi, J. M. Finn, C. E. Hyde-Wright, R. W. Lourie, B. E. Norum, P. E. Ulmer, and B. L. Berman, Phys. Rev. C **43**, 2103 (1991).

[7] H. Seifert, Ph.D. thesis, University of Maryland, 1990.

[8] T. Cheon, K. Takayanagi, and K. Yazaki, Nucl. Phys. **A437**, 301 (1985); **A445**, 227 (1985).

[9] T. Cheon and K. Takayanagi, Nucl. Phys. **A455**, 653 (1986).

[10] J. P. Jeukenne, A. Lejeune, and C. Mahaux, Phys. Rev. C **10**, 1391 (1974).

[11] J. P. Jeukenne, A. Lejeune, and C. Mahaux, Phys. Rep. **25**, 83 (1976); Phys. Rev. C **15**, 10 (1977); **16**, 80 (1977).

[12] F. A. Brieva and J. R. Rook, Nucl. Phys. **A291**, 299 (1977); **A291**, 317 (1977); **A297**, 206 (1978); **A307**, 493 (1978).

[13] H. V. von Geramb, in *The Interaction Between Medium Energy Nucleons in Nuclei (Indiana Cyclotron Facility, Bloomington, Indiana)*, Proceedings of the Workshop on the Interaction Between Medium Energy Nucleons in Nuclei, AIP Conf. Proc. No. 97, edited by H. O. Meyer (AIP, New York, 1982), p. 44.

[14] L. Rikus, K. Nakano, and H. V. von Geramb, Nucl. Phys. **A414**, 413 (1984).

[15] K. Nakayama and W. G. Love, Phys. Rev. C **38**, 51 (1988).

[16] L. Ray, Phys. Rev. C **41**, 2816 (1990).

[17] J. Hüfner and C. Mahaux, Ann. Phys. **73**, 525 (1972).

[18] L. G. Arnold, B.C. Clark, R. L. Mercer, and P. Schwandt, Phys. Rev. C **23**, 1949 (1981); L. G. Arnold, B.C. Clark, and R. L. Mercer, *ibid.* **23**, 15 (1981).

[19] J. A. McNeil, L. Ray, and S. J. Wallace, Phys. Rev. C **27**, 2123 (1983).

[20] M. V. Hynes, A. Picklesimer, P. C. Tandy, and R. M. Thaler, Phys. Rev. Lett. **52**, 978 (1984); Phys. Rev. C **31**, 1438 (1985).

[21] N. Ottenstein, S. J. Wallace, and J. A. Tjon, Phys. Rev. C **38**, 2272 (1988); **38**, 2289 (1988).

[22] S. Hama, B. C. Clark, E. D. Cooper, H. S. Sherif, and R. L. Mercer, Phys. Rev. C **41**, 2737 (1990).

[23] C. W. Glover, P. Schwandt, H. O. Meyer, W. W. Jacobs, J. R. Hall, M. D. Kaitchuck, and R. P. de Vito, Phys. Rev. C **31**, 1 (1985).

[24] E. J. Stephenson, J. Phys. Soc. Jpn. (Suppl.) **55**, 316 (1985); P. Schwandt (private communication).

[25] J. J. Kelly, computer code ALLFIT (unpublished).

[26] J. J. Kelly, Ph.D. thesis, Massachusetts Institute of Technology, 1981.

[27] M. V. Hynes, J. J. Kelly, B. W. Peterson, and B. E. Norum (unpublished).

[28] S. Dixit, Master's thesis, Massachusetts Institute of Technology, 1986.

[29] J. P. Glickman, W. Bertozzi, T. N. Buti, S. Dixit, F. W. Hersman, C. E. Hyde-Wright, M. V. Hynes, R. W. Lourie, B. E. Norum, J. J. Kelly, B. L. Berman, and D. J. Millener, Phys. Rev. C **43**, 1740 (1991).

[30] S. Dixit, W. Bertozzi, J. M. Finn, F. W. Hersman, C. E. Hyde-Wright, M. V. Hynes, M. A. Kovash, B. E. Norum, A. D. Bacher, G. T. Emery, C. C. Foster, W. P. Jones, D. W. Miller, B. L. Berman, J. J. Kelly, and D. J. Millener, Phys. Rev. C **43**, 1758 (1991).

[31] T. N. Buti, J. J. Kelly, W. Bertozzi, J. M. Finn, F. W. Hersman, C. Hyde-Wright, M. V. Hynes, M. A. Kovash, S.j Kowalski, R. W. Lourie, B. Murdock, B. E. Norum, B. Pugh, C. P. Sargent, W. Turchinetz, and B. L. Berman, Phys. Rev. C **33**, 755 (1986).

[32] F. Ajzenberg-Selove, Nucl. Phys. **A460**, 1 (1986); **A490** 1 (1988).

[33] P. M. Endt and C. van der Leun, Nucl. Phys. **A310**, 1 (1978).

[34] J. J. Kelly, Phys. Rev. C **46**, 711 (1992).

[35] See AIP document no. PAPS PRVCA-47-1615 for 55 pages containing a complete tabulation of the data described in this paper. Order by PAPS number and journal reference from American Institute of Physics, Physics Auxiliary Publication Service, 335 E. 45th Street, New York, NY 10017. The price is $1.50 for each microfiche or $8.75 for photocopies. Airmail additional. Make checks payable to the American Institute of Physics.

[36] G. Lahm, Ph.D. thesis, University of Mainz, 1982.

[37] H. J. Emrich, Ph.D. thesis, University of Mainz, 1983.

[38] R. A. Miskimen, Ph.D. thesis, Massachusetts Institute of Technology, 1983.

[39] P. Harihar, K. K. Seth, D. Barlow, S. Iversen, M. Kaletka, H. Nann, A. Saha, C. F. Williamson, J. W. Wong, M. Deady, and W. J. Gerace, Phys. Rev. Lett. **53**, 152 (1984).

[40] F. Petrovich, R. J. Philpott, A. W. Carpenter, and J. A. Carr, Nucl. Phys. **A425**, 609 (1984).

[41] J. A. Carr, F. Petrovich, and J. J. Kelly, in *Neutron-Nucleus Collisions—A Probe of Nuclear Structure (Burr Oak State Park, Glouster, Ohio, 1984)*, Proceedings of the Conference on Neutron-Nucleus Collisions—A Probe of Nuclear Structure, AIP Conf. Proc. No. 124, edited by J. Rapaport, R. W. Finlay, S. M. Grimes, and F. S. Dietrich (AIP, New York, 1984), p. 230.

[42] A. K. Kerman, H. McManus, and R. M. Thaler, Ann. Phys. **8**, 551 (1959).

[43] W. G. Love and M. A. Franey, Phys. Rev. C **24**, 1073 (1981).

[44] F. Petrovich, H. McManus, V. A. Madsen, and J. Atkinson, Phys. Rev. Lett. **22**, 895 (1969).

[45] M. Lacombe, B. Loiseau, J. M. Richard, R. Vinh Mau, J. Cote, P. Pires, and R. de Tourreil, Phys. Rev. C **21**, 861 (1980).

[46] H. V. von Geramb, F. A. Brieva, and J. R. Rook, in *Microscopic Optical Potentials*, edited by H. V. von Geramb (Springer-Verlag, Berlin, 1979), p. 104.

[47] P. J. Siemens, Nucl. Phys. **A141**, 225 (1970).

[48] R. Machleidt, K. Holinde, and Ch. Elster, Phys. Rep. **149**, 1 (1987).
[49] K. M. Watson, Phys. Rev. **89**, 575 (1953).
[50] L. Ray, Phys. Rev. C **35**, 1072 (1987).
[51] E. L. Lomon and H. Feshbach, Ann. Phys. (N.Y.) **48**, 94 (1968).
[52] E. L. Lomon, Phys. Rev. D **26**, 576 (1982).
[53] E. Clementel and C. Villi, Nuovo Cimento **2**, 176 (1955).
[54] R. A. Arndt, L. D. Roper, R. A. Bryan, R. B. Clark, B. J. VerWest, and P. Signell, Phys. Rev. D **32**, 128 (1987); R. A. Arndt, J. S. Hyslop, III, and L. D. Roper, *ibid.* **35**, 128 (1987); R. A. Arndt and L. D. Roper, *Scattering Analysis Interactive Dial-in SAID* (Virginia Polytechnic Institute, Blacksburg, 1988).
[55] M. A. Franey and W. G. Love, Phys. Rev. C **31**, 488 (1985).
[56] F. Petrovich, J. A. Carr, R. J. Philpott, A. W. Carpenter, and J. Kelly, Phys. Lett. **165B**, 19 (1985).
[57] H. F. Arellano, F. A. Brieva, and W. G. Love, Phys. Rev. C **41**, 2188 (1990).
[58] Ch. Elster, T. Cheon, E. F. Redish, and P.C. Tandy, Phys. Rev. C **41**, 814 (1990).
[59] R. Crespo, R. C. Johnson, and J. A. Tostevin, Phys. Rev. C **41**, 2257 (1990).
[60] H. O. Meyer, P. Schwandt, G. L. Moake, and P. P. Singh, Phys. Rev. C **23**, 616 (1981); H. O. Meyer, J. Hall, W. W. Jacobs, P. Schwandt, and P. P. Singh, Phys. Rev. C **24**, 1782 (1981).
[61] D. A. Hutcheon *et al.*, in *Polarization Phenomena in Nuclear Physics-1980 (Fifth International Symposium, Sante Fe)*, Proceedings of the Fifth International Symposium on Polarization Phenomena in Nuclear Physics, AIP Conf. Proc. No. 69, edited by G. G. Ohlsen, R. E. Brown, N. Jarmie, W. W. McNaughton, and G. M. Hale (AIP, New York, 1981).
[62] M. Ju, M.S. thesis, Simon Fraser University, 1987 (unpublished).
[63] L. Ray and G.W. Hoffman, Phys. Rev. C **31**, 538 (1985); L. Ray (private communication).
[64] D. P. Murdock and C. J. Horowitz, Phys. Rev. C **35**, 1442 (1987).